Kaunas University of Technology

Faculty of Mechanical Engineering and Design

Development of a Remote Structural Health Monitoring System for Unmanned Aircraft

Master's Final Degree Project

Gabrielė Jovarauskaitė

Project author

Assist. Gediminas Monastyreckis

Supervisor

Kaunas, 2025

Kaunas University of Technology

Faculty of Mechanical Engineering and Design

Development of a Remote Structural Health Monitoring System for Unmanned Aircraft

Masters's Final Degree Project

Aeronautical Engineering (6211EX024)

Gabrielė Jovarauskaitė

Project author

Assist. Gediminas Monastyreckis

Supervisor

Assist. Joris Vėžys

Reviewer

Kaunas, 2025

Kaunas University of Technology
Faculty of Mechanical Engineering and Design
Gabrielė Jovarauskaitė

Development of a Remote Structural Health Monitoring System for Unmanned Aircraft

Declaration of Academic Integrity

I confirm the following:

1. I have prepared the final degree project independently and honestly without any violations of the copyrights or other rights of others, following the provisions of the Law on Copyrights and Related Rights of the Republic of Lithuania, the Regulations on the Management and Transfer of Intellectual Property of Kaunas University of Technology (hereinafter – University) and the ethical requirements stipulated by the Code of Academic Ethics of the University;

2. All the data and research results provided in the final degree project are correct and obtained legally; none of the parts of this project are plagiarised from any printed or electronic sources; all the quotations and references provided in the text of the final degree project are indicated in the list of references;

3. I have not paid anyone any monetary funds for the final degree project or the parts thereof unless required by the law;

4. I understand that in the case of any discovery of the fact of dishonesty or violation of any rights of others, the academic penalties will be imposed on me under the procedure applied at the University; I will be expelled from the University and my final degree project can be submitted to the Office of the Ombudsperson for Academic Ethics and Procedures in the examination of a possible violation of academic ethics.

Gabrielė Jovarauskaitė

Confirmed electronically

Kaunas University of Technology

Faculty of Mechanical Engineering and Design

Task of the Master's Final Degree Project

Given to the student – Gabrielė Jovarauskaitė

1. Topic of the project

Development of a Remote Structural Health Monitoring System for Unmanned Aircraft

(In English)

Bepiločių orlaivių nuotolinės struktūrinės būklės stebėsenos sistemos kūrimas

(In Lithuanian)

2. Aim and tasks of the project

Aim:
Develop a sandwich-structured composite with an integrated wireless self-sensing system for structural health monitoring.
Tasks:
1. Develop self-sensing sandwich-structured composites with an electrically conductive honeycomb core.
2. Perform analytical electromechanical modelling to predict changes in electrical response under mechanical loads and assess the sensitivity of the composite to damage.
3. Perform tests on temperature fluctuations, localised compression, three-point bending, and delamination to evaluate the composite's durability and self-diagnostic performance.
4. Manufacture a wing prototype with an integrated wireless self-diagnostic system and monitor the composite structural integrity in real time.

3. Main requirements and conditions

The detection system must accurately locate damage in real time, by measuring local changes in electrical resistance.

4. Additional requirements and conditions for the project, report and appendices

Not applicable

Project author	Gabrielė Jovarauskaitė	15-02-2025
	(Name, Surname)	*(Date)*
Supervisor	Gediminas Monastyreckis	15-02-2025
	(Name, Surname)	*(Date)*
Head of study field programs	Prof. Artūras Keršys	15-02-2025
	(Name, Surname)	*(Date)*

Jovarauskaitė, Gabrielė. Development of a Remote Structural Health Monitoring System for Unmanned Aircraft. Master's Final Degree Project / supervisor Assist. Gediminas Monastyreckis; Faculty of Mechanical Engineering and Design, Kaunas University of Technology.

Study field and area (study field group): Aeronautical Engineering (E14), Engineering Science.

Keywords: structural health monitoring, self-sensing composites, nanoparticles.

Kaunas, 2025. 55.

Summary

This study investigates the application of electrically conductive sandwich-structured composites with an aramid honeycomb core for damage monitoring in unmanned aerial vehicles (UAVs). Honeycomb cores are susceptible to failure modes such as buckling, wrinkling, and delamination, which are difficult to detect using conventional damage detection methods. Various techniques have been applied in the aerospace industry, including fibre optics, accelerometers, and piezoelectric sensors. Although effective in some applications, these systems are often expensive, complex, and have limited ability to detect internal damage within the honeycomb core. To address these limitations, this study explores the use of electrically conductive nanoparticles for structural health monitoring (SHM). When embedded into a composite, conductive networks exhibit a piezoresistive effect – mechanical damage leads to an increase in electrical resistance, which can be measured.

Specimens consisted of an aramid honeycomb coated with MXene nanoparticles and six layers of glass fibre, one of which was covered with carbon nanotubes. Additionally, carbon fibre threads and unidirectional carbon fibre were integrated into the composite to measure local electrical resistance using a multimeter. Following electrical measurements of the individual components (honeycomb and glass fibre), an analytical model based on Ohm’s law was developed. The model demonstrated that the sensitivity of the electrical resistance of the composite depends on the relative conductivity of the individual layers. Composites were tested for compression, three-point bending, delamination, and temperature. During compression testing, when a local indentation 4 mm deep was introduced, the highest resistance change was recorded closer to the measurement channel due to defects in the conductive nanoparticle network. The delamination tests showed that, as the upper glass fibre layer was gradually separated from the honeycomb, the composite resistance increased exponentially. Three-point bending tests revealed a correlation between resistance change and deflection size. As the temperature varied from –14 °C to +70 °C, the relative resistance of the composite decreased by 50%. Furthermore, the study presents a 13 × 27 cm composite wing prototype equipped with six measurement channels connected to an “Arduino Nano ESP32“ microcontroller. The system measures electrical resistance in the channels in real-time and transmits the data wirelessly via Wi-Fi to the “Arduino IoT Cloud Remote” mobile application, where damage initiation and propagation can be graphically monitored. This technology enables the identification of honeycomb damage, fibre delamination, local cracks, and indentations.

Jovarauskaitė, Gabrielė. Bepiločių orlaivių nuotolinės struktūrinės būklės stebėsenos sistemos kūrimas. Magistro baigiamasis projektas / Asist. Gediminas Monastyreckis; Kauno technologijos universitetas, Mechanikos inžinerijos ir dizaino fakultetas.

Studijų kryptis ir sritis (studijų krypčių grupė): Aeronautikos inžinerija (E14), Inžinerijos mokslai.

Reikšminiai žodžiai: struktūros būklės stebėsena, savidiagnostiniai kompozitai, nanodalelės.

Kaunas, 2025. 55. p.

Santrauka

Šiame darbe nagrinėjamas elektrai laidžių sumuštinio tipo kompozitų, su aramido korio tipo šerdimi, taikymas pažeidimų stebėsenai nepilotuojamuosiuose orlaiviuose (UAV). Korio tipo šerdis yra jautri tam tikriems pažeidimų tipams, tokiems kaip gniuždymas, bangavimas ir atsisluoksniavimas, kurių aptikimas taikant įprastus diagnostikos metodus yra sudėtingas. Aviacijos pramonėje taikomi įvairūs pažeidimų aptikimo metodai, įskaitant optines skaidulas, akselerometrus bei pjezoelektrinius jutiklius. Nors šios sistemos veiksmingos tam tikrose srityse, jos dažnai yra brangios, sudėtingos ir ribotai pajėgios aptikti vidinius pažeidimus korinėse struktūrose. Siekiant įveikti šiuos trūkumus, darbe tiriamas elektrai laidžių nanodalelių taikymas struktūrinės būklės stebėsenai (SHM). Įterpus tokias daleles į kompozitą, suformuojami laidūs tinklai, pasižymintys piezorezistiniu efektu – mechaniniai pažeidimai sukelia elektrinės varžos padidėjimą, kurį galima išmatuoti.

Bandiniai buvo sudaryti iš aramido korio, padengto makseno nanodalelėmis, ir šešių stiklo pluošto sluoksnių, iš kurių vienas – padengtas anglies nanovamzdeliais. Be to, kompozito struktūroje buvo integruoti anglies pluošto gijos ir vienakryptis anglies pluoštas, skirti lokalios elektrinės varžos matavimui multimetru. Atlikus atskirų komponentų (korio ir stiklo pluošto) elektrinius matavimus, buvo sudarytas analitinis modelis, pagrįstas Omo dėsniu. Modelis parodė, kad kompozito varžos jautrumas priklauso nuo atskirų sluoksnių santykinio elektrinio laidumo. Su kompozitais buvo atlikti gniuždymo, tritaškio lenkimo, atsisluoksniavimo ir temperatūriniai bandymai. Gniuždymo bandymo metu, suformavus 4 mm gylio lokalų įspaudimą, didžiausias varžos pokytis buvo užfiksuotas arčiau matavimo kanalo dėl laidžių nanodalelių tinklelio defektų. Atsisluoksniavimo bandymų rezultatai pademonstravo, kad palaipsniui atsiskiriant viršutiniam stiklo pluošto sluoksniui nuo korio, kompozito varža didėjo eksponentiškai. Tritaškio lenkimo bandymai parodė varžos pokyčio priklausomybę nuo įlinkio dydžio. Kintant temperatūrai nuo –14 °C iki +70 °C, kompozito santykinė varža sumažėjo 50 %. Taip pat darbe pristatytas 13 × 27 cm dydžio kompozitinio sparno prototipas su 6 matavimo kanalais, prijungtais prie „Arduino Nano ESP32“ mikrovaldiklio. Sistema realiuoju laiku matuoja elektrinę varžą kanaluose ir belaidžiu Wi-Fi ryšiu perduoda duomenis į mobiliąją programėlę „Arduino IoT Cloud Remote“, kurioje galima grafiškai stebėti pažeidimų atsiradimą ir jų plitimą. Ši technologija leidžia aptikti korio pažeidimus, pluoštų atsisluoksniavimą, lokalius įtrūkius ir įspaudimus.

Table of contents

List of figures

List of tables

List of abbreviations

Abbreviations:

CF – carbon fibre;

CNT – carbon nanotubes;

GF – glass fibre;

MWCNT – multi wall carbon nanotubes;

SHM – structural health monitoring;

SWCNT – single wall carbon nanotubes;

UAV – unmanned aerial vehicle;

UCF – unidirectional carbon fibre.

Introduction

Due to their great weight and strength ratio, composites are used in drone structures. Despite the significant advantages of composites, they are sensitive to defects such as cracks, debonding, delamination, and fibre breakage. After numerous flight cycles, unnoticed weaknesses can lead to structural integrity failure, ultimately affecting aircraft safety. It is crucial to identify these defects early to prevent such failures [1]. The condition of the drone structure is periodically checked during maintenance with the help of non-destructive (NDT) or structural health monitoring (SHM) methods using sensors such as strain gauges and optical fibres. However, these methods are limited by time and resources [2]. Another SHM technique is based on self-sensing composites. They include electrically conductive additives, which create a piezoresistive effect and can indicate potential structural damage. Therefore, such composites are a viable solution for drone structures where early-stage damage monitoring is necessary [3].

This study aims to develop a self-sensing sandwich-structured composite for structural health monitoring. The investigated composite consists of an electrically conductive honeycomb core dip-coated with MXenes, a carbon nanotubes (CNT) spray-coated glass fibre interlayer, and a unidirectional carbon fibre interlayer. The piezoresistive response of the composite was evaluated through indentation, delamination, three-point bending, and temperature variation tests. A wing prototype incorporating the sandwich-structured composite was also fabricated and equipped with a real-time resistance monitoring system. The results demonstrated that nanoparticle-modified sandwich composites enable complex damage detection, including core buckling, fibre cracking, and interlaminar debonding making them highly suitable for real-time monitoring of aircraft structures.

The aim of this study is to develop a sandwich-structured composite with an integrated wireless self-sensing system for structural health monitoring.

The tasks are:

1. Develop self-sensing sandwich-structured composites with an electrically conductive honeycomb core.
2. Perform analytical electromechanical modelling to predict changes in electrical response under mechanical loads and assess the composite's sensitivity to damage.
3. Perform tests on temperature fluctuations, localised compression, three-point bending, and delamination to evaluate the composite's durability and self-diagnostic performance.
4. Manufacture a wing prototype with an integrated wireless self-diagnostic system and monitor the composite structural integrity in real time.

1. Literature review

1.1. Unmanned aerial vehicle (UAV)

The International Civil Aviation Organization (ICAO) defines a drone, also known as an unmanned aerial vehicle (UAV), as an aircraft that operates without a human pilot on board. In other words, a drone is either remotely controlled by an operator on the ground or pre-programmed to follow specific flight routes [4].

Drones can perform automated tasks and collect real-time data, making them highly desirable in various industries, including agriculture, healthcare, construction, and the military. They can undertake missions that are often unsuitable or too risky for manned aircraft. For instance, during dull missions, drones can provide long-endurance surveillance or atmospheric monitoring; in dirty missions, they can operate in hazardous environments such as those containing radiation, biological agents, or chemical hazards; and in dangerous missions (such as aerial combat, target strikes, or suppression of enemy air defences) they can minimise risk to human life. The wide range of drone types allows them to be tailored to specific missions, each with unique strengths and limitations [5].

1.1.1. UAV types

There are three main types of drones: fixed-wing, rotary-wing, and hybrid drones (Fig. 1). One of the most used UAV type is the multi-rotor drone, which is further divided based on the number of rotors: tricopters, quadcopters, hexacopters, and octocopters. They can also be classified based on their size and payload capacity. Multi-rotor drones are constructed with multiple rotors symmetrically arranged around a lightweight frame. These rotors generate thrust and are controlled by electronic speed controllers using pulse-width modulation. Flight direction is achieved by varying the speed of individual rotors – a configuration that allows for excellent control, stability, and omnidirectional movement. Their power source is typically a lithium polymer battery, offering a good power-to-weight ratio. However, battery capacity limits their flight performance to approximately 5–20 minutes. Inertial measurement units (gyroscopes and accelerometers) are used to estimate orientation, which is essential for stable flight, particularly for autonomous drones [6,7].

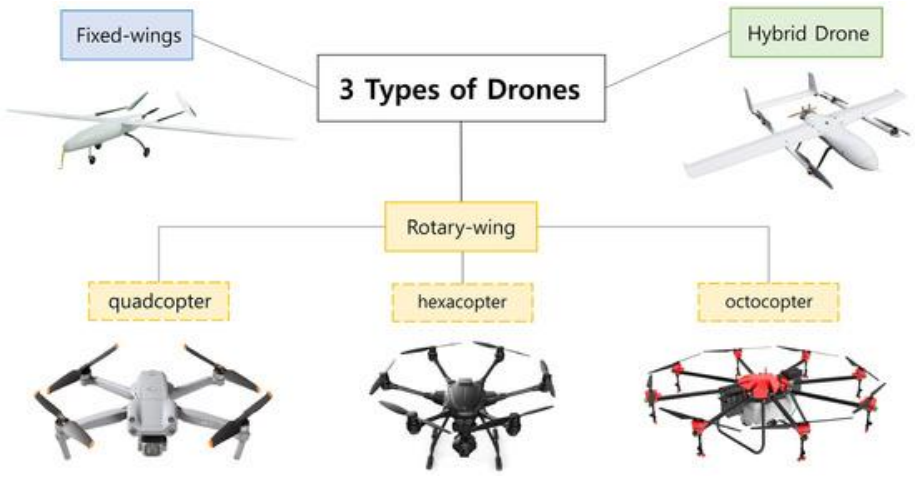

Fig. 1. Main types of drones: fixed-wing, rotary-wing, and hybrid UAVs [6]

Rotary-wing drones are known for their compact size, ease of control, and affordability, which makes them popular not only in military use but also in civilian sectors. They offer excellent positional

control and stability, making them ideal for tasks such as aerial photography, cinematography, mapping, and infrastructure inspection. The quadcopter is the most popular variant due to its ability to hover steadily and manoeuvre precisely, making it ideal for capturing both stable and dynamic visuals. In agriculture, drones are employed for vegetation analysis, crop health monitoring, and precision pesticide spraying, helping farmers increase efficiency, reduce chemical usage, and minimise crop damage. Additionally, they can be used for monitoring the structural health of hard-to-reach buildings, bridges, and other infrastructure. Furthermore, drones play a vital role in research fields such as wildfire surveillance, air quality sampling, and search-and-rescue operations. Their modularity and versatility enable customisation for different payloads and missions across various industries [7].

Fixed-wing UAVs are similar in design to traditional airplanes, where lift is generated through forward motion. Structurally, they consist of a fuselage, fixed wings, tail section, landing gears, and one or more propulsion units (either electric or fuel-powered) mounted at the front or rear (Fig. 2a). Unlike multi-rotor drones, they lack vertical lift mechanisms and are designed primarily for efficient, long-range, and high-endurance missions. This is attributed to their aerodynamic structure, which allows for significantly reduced power consumption during flight. Their glide capability also enables continued flight during power failures, enhancing operational safety. Control surfaces, such as ailerons, elevators, and rudders, allow for roll, pitch, and yaw control, improving manoeuvrability in forward flight [8,9].

However, fixed-wing drones also have limitations. They require runways for take-off and landing, cannot hover or perform vertical landings, and typically require more extensive pilot training. Their structural complexity and material choices also contribute to higher manufacturing and maintenance costs. Despite these challenges, their ability to carry heavier payloads, travel long distances, and maintain flight for extended durations makes them indispensable for missions where endurance, speed, and efficiency are paramount. Consequently, they are used across multiple sectors including aerial mapping, border patrol, environmental monitoring, and military reconnaissance. They can also be deployed in cooperative drone systems, where multiple UAVs operate under a coordinated control strategy to perform complex tasks more efficiently than a single UAV could [8,9].

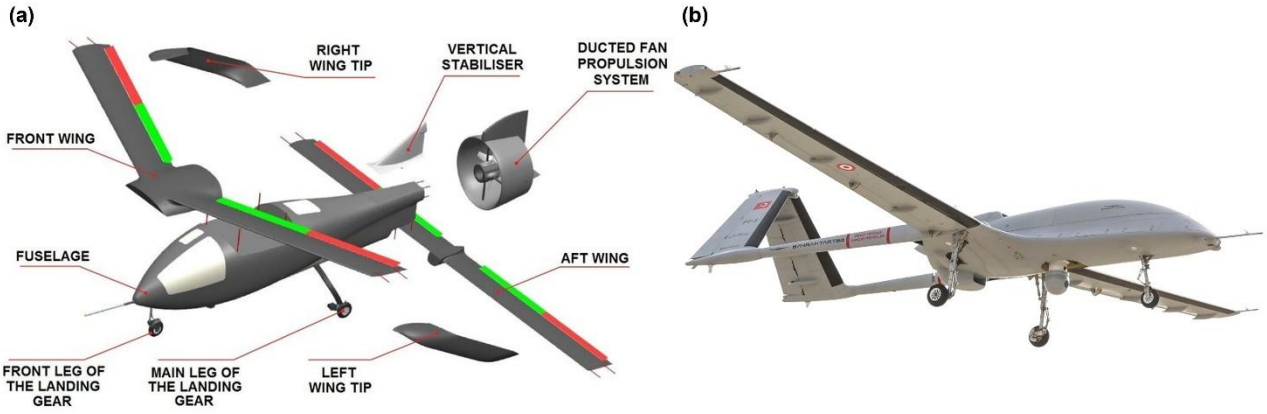

Fig. 2. Fixed-wing UAV: (a) structure [10]; (b) “Bayraktar TB3“ military drone [11]

Military drones have become a crucial tool for intelligence gathering, executing precise strikes, and enhancing national security. Modern military UAVs are equipped with advanced cameras and sensors, enabling real-time monitoring in hazardous areas. They are widely used for surveillance,

spying on enemy activity, and launching accurate strikes while minimising risks to personnel. Figure 2b shows the “Bayraktar TB3“fixed-wing military drone, an advanced unmanned combat aerial vehicle designed for long-endurance operations and equipped with cutting-edge surveillance, reconnaissance, and strike capabilities. Developed by “Baykar“, the “TB3“ features foldable wings for naval operations and can carry precision-guided munitions, making it highly adaptable for both land-based and aircraft carrier deployments [12].

Hybrid UAVs represent a drone class that combines the benefits of both fixed-wing and rotary-wing aircraft – vertical take-off and landing (VTOL) capabilities along with efficient long-distance forward flight. This integration allows for a broader flight envelope, covering vertical lift, cruise, and smooth transitions between modes. This makes hybrid UAVs especially suitable for missions requiring both long-range efficiency and high manoeuvrability. However, their design is more complex due to the integration of components from both drone types. Their architecture typically includes rigid airframes, lifting wings, rotors or propellers, tilting mechanisms, and reinforced landing structures [13].

Hybrid UAVs can be categorised into two types: convertiplanes and tail-sitters (Fig. 3). Convertiplanes include mechanisms that change the orientation of rotors or wings to enable transitions between vertical and horizontal flight. These UAVs typically feature a fuselage that contains the avionics, payload, and power systems, along with side-mounted wings and mechanically tilting nacelles positioned at the wing tips. The nacelles allow the rotors to rotate between vertical and horizontal configurations. These tilting components must be structurally reinforced to endure aerodynamic and inertial loads during transition. In contrast, tail-sitter UAVs eliminate the need for tilt mechanisms, resulting in a simpler and more compact design. They have fixed wings and multiple rotors arranged symmetrically along the airframe. These UAVs take off and land vertically on their tails, transitioning into cruise flight by pitching the entire body forward. This configuration demands a rigid and well-balanced fuselage capable of withstanding both gyroscopic forces and aerodynamic stresses during the manoeuvre [13].

Fig. 3. Hybrid UAVs: convertiplanes and tail-sitter [10]

Hybrid UAV platforms are employed in military missions involving intelligence, surveillance, reconnaissance, and precision strikes due to their ability to operate from unprepared sites and sustain long-endurance flights. Civilian applications include parcel delivery, disaster response, infrastructure inspection, search and rescue, and agricultural monitoring [13].

1.1.2. Materials used in UAVs

A key requirement for UAV materials is the combination of strength, stiffness, weight, cost, and manufacturability. The three main classes of materials include metals, wood, and composites. Metals such as aluminium, titanium, and steel are the most common structural materials in traditional aircraft design. Aluminium alloys are favoured for their excellent strength-to-weight ratio, easy manufacturing, corrosion resistance, and widespread availability. These properties make aluminium suitable for spars, skin panels, and fuselage elements, especially in manned aircraft. However, in UAVs, metals are often replaced by composites, which offer better weight savings for the same strength, while modern UAVs typically do not require the extremely high structural robustness that manned aircraft demand [5].

The most used fibre types in UAV applications are carbon fibre, aramid, and glass fibre. Their mechanical properties are shown in Table 1. Carbon fibre offers the highest stiffness and strength among these materials and is widely used in structural components such as wings, fuselages, and control surfaces. It allows a reduction in structural weight by 25–30% compared to traditional metallic constructions, which enables greater payload capacity or extended flight duration. Aramid fibres are valued for their toughness and resistance to impact and ballistic threats. These are particularly useful in UAVs that are subject to rough landings or crash scenarios. Aramid's low density also contributes to mass savings. Glass fibre is less strong than carbon or aramid but is cost-effective and sufficient for components that do not experience high structural loads. It is commonly used in radomes, fairings, and non-critical wing skins [5].

Table 1. Properties of fibre/epoxy plies [5]

Material	**Tensile Strength σ_{tu}, MPa**	**Shear Strength τ_u, MPa**	**Young's Modulus E, GPa**	**Shear Modulus G, GPa**	**Density ρ, kg/m³**
Carbon-epoxy	1270	63	7	4.2	1530
Glass-epoxy	1250	63	12	4.5	2080
Aramid-epoxy	1410	45	5.6	2.1	1350

The wing is one of the most critical structural elements in any fixed-wing UAV, as it creates the majority of aerodynamic forces during cruise, take-off, and landing. The wing structure has to withstand these forces while minimising weight. Therefore, sandwich composites can be used to improve bending stiffness without significantly increasing mass [14]. For instance, the "NRL SENDER" UAV's wing is fabricated as a moulded glass fiber sandwich wing with carbon reinforcement [5].

1.2. Sandwich-structured composites

Sandwich-structured composites consist of a lightweight core material bonded between two thin, stiff face sheets, also referred to as skins. Bonding is typically achieved using adhesive films or through co-curing processes. The face sheets, commonly made from materials such as aluminium, carbon

fibre, or glass fibre-reinforced polymers, are responsible for carrying the in-plane tensile and compressive loads, as illustrated in Fig. 4. The core, which is thicker yet significantly lighter, plays a critical role in resisting shear forces, preventing wrinkling of the face sheets, and distributing applied loads and stresses. This design results in structures with high strength-to-weight and stiffness-to-weight ratios [15,16].

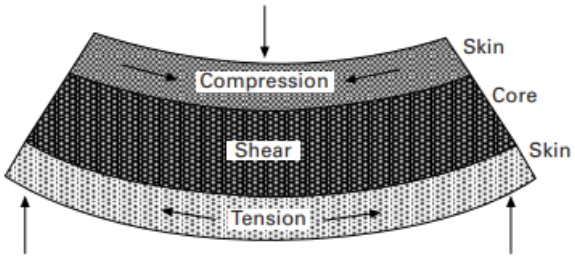

Fig. 4. Load distribution in a sandwich-structured composite [17]

1.2.1. Core materials

Sandwich composites are often classified based on the type of core material employed. The most used core types include foam, honeycomb, folded, and lattice structures. Each core design offers specific mechanical and structural properties tailored to different applications. Honeycomb cores, whether metallic or non-metallic, are widely recognised for their high strength-to-weight and stiffness-to-weight ratios, as well as their ability to distribute loads efficiently. However, their open-cell geometry provides limited bonding area with the face sheets, which may reduce interfacial strength. Additionally, they tend to exhibit sensitivity to moisture absorption, corrosion and possess relatively low lateral strength, making them vulnerable to collapse during forming or curing. Foam cores are frequently used in the aerospace industry due to their low weight, good energy absorption capacity, and relatively low manufacturing costs. They offer high specific bending strength and compressive resistance, although their shear strength is lower compared to honeycomb cores. Furthermore, foams may trap moisture and often display variability in their structure, necessitating conservative design approaches. Folded cores are manufactured by folding flat sheets into predetermined patterns, which allows for cost-effective, continuous production. Their open-cell structure enhances ventilation and moisture resistance. Nonetheless, the manufacturing process demands high geometric accuracy, and the complexity of the folded geometry makes mechanical modelling more difficult. Lattice cores are made from a three-dimensional network of interconnected struts, forming a truss-like architecture. These cores are notable for their tuneable geometry, which enables designers to optimise the structure for specific loading scenarios. Although they provide outstanding strength and stiffness at minimal weight, lattice cores are challenging to design and fabricate and are prone to defects resulting from their intricate geometry [16,18]. In the aviation industry, the need to achieve high strength and stiffness while minimising weight has led to the widespread use of Nomex honeycomb, aluminium honeycomb, and foam cores. Although foam cores offer better moisture resistance and reduced production costs, their mechanical strength remains lower than that of honeycomb variants, which are used where performance is critical [19].

Nomex honeycomb cores are manufactured using the expansion method, illustrated in Fig. 5. This process begins with aramid foil sheets being printed or coated with adhesive lines at precise intervals. These sheets are then cut to the required length, stacked, and pressed together to form a block. After

partial curing of the adhesive, the block is mechanically expanded, which creates the hexagonal cell structure characteristic of honeycomb cores. The next step involves resin impregnation, which significantly improves mechanical strength, thermal stability, fire retardancy, and resistance to moisture. Following resin application, the core undergoes a controlled curing process in an oven, ensuring that the desired structural properties are achieved. The final step involves slicing the cured block into sheets of the required thickness [16,20].

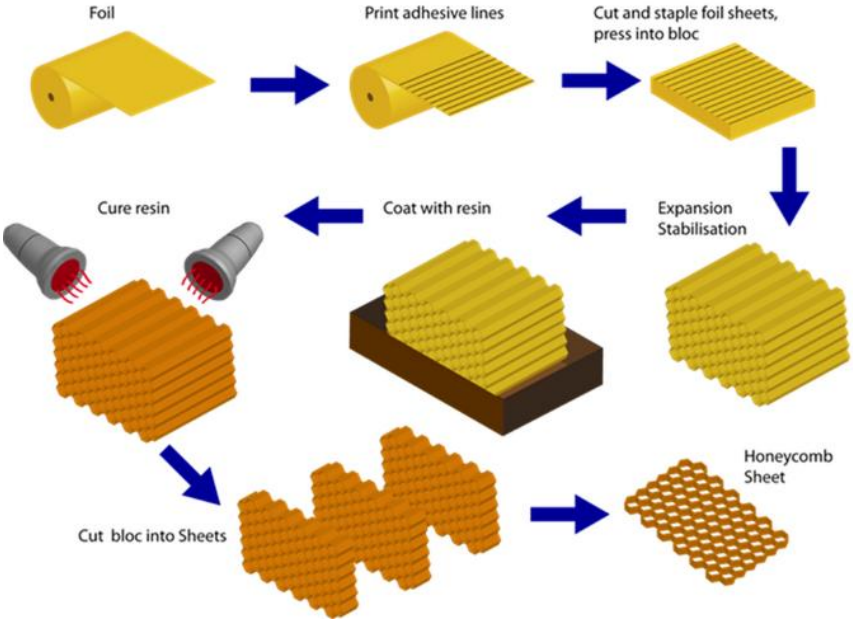

Fig. 5. Nomex honeycomb manufacturing process [21]

The honeycomb cell walls, as shown in Fig. 6, are composed of aramid paper bonded with phenolic resin. Although phenolic resin provides good fire resistance and mechanical stability, it is porous and hygroscopic, meaning it tends to absorb moisture over time. Moreover, the honeycomb structure itself is rough, porous, and hydrophilic, further contributing to moisture absorption. [22].

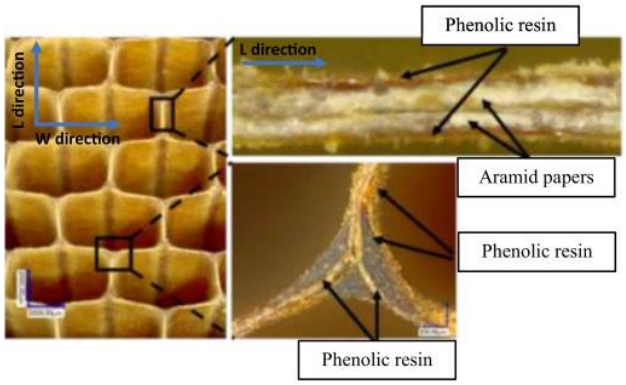

Fig. 6. Composition of the Nomex honeycomb structure [22]

This ability to absorb moisture can be used to add nanoparticles into the honeycomb. For example, MXene nanosheets can be added by dipping the honeycomb into a water-based MXene solution. This improves the honeycomb's strength and makes it electrically conductive, which allows it to be used in more advanced applications [23].

1.2.2. Failures in honeycomb

When compared to traditional stiffened panels, sandwich composites offer several advantages, including reduced weight, increased stiffness, and simpler, faster manufacturing processes. However, they also have two key limitations: the core material is generally weaker than the face sheets, and the adhesive bond between the core and skins is a common failure point. These weaknesses can lead to damage such as localised crushing, cracking, delamination, and fibre breakage [17,24].

When a sandwich structure experiences localised loading such as from an impact or indentation the damage typically initiates in the face sheets, which bend and transfer the load to the core. The response of the structure largely depends on the type of core material. Metallic cores, due to their higher stiffness, often result in permanent dents (Fig. 7a). A weak adhesive interface between a metallic core and the face sheets may encourage debonding, leaving areas of the skin unsupported (Fig. 7b). In contrast, non-metallic honeycomb cores are more compliant, tend to deform more under load, and often cause the face sheet to wrinkle, as seen in Fig. 7c [13].

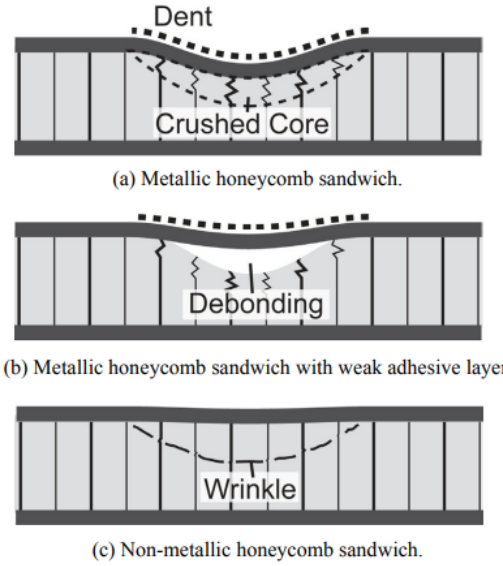

Fig. 7. Impact damage in different types of honeycomb sandwich structures [17]

If such damage remains undetected and the structure continues to operate under cyclic loading conditions, the structural integrity can further degrade. As the core loses its load-supporting capacity, the face sheets may begin to buckle. Simultaneously, adhesive layer failures such as debonding or cracking can lead to delamination between the face sheets and the core, a failure pattern illustrated in Fig. 8 [17,24].

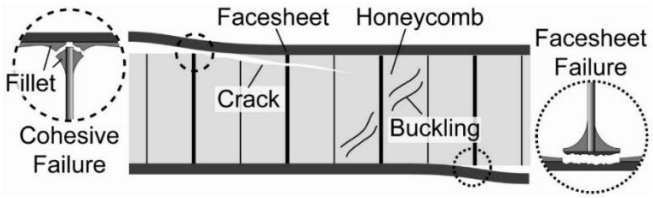

Fig. 8. Common failure modes in sandwich-structured composites [24]

A particularly challenging form of damage in sandwich composites used in aerospace applications is interlaminar damage. Unlike surface defects, which can often be identified visually, interlaminar

damage, including delamination, matrix cracking, and fibre–matrix debonding, typically occurs internally and is difficult to detect using traditional non-destructive inspection (NDT) methods. These techniques are often ineffective due to the low density of the core materials. As these hidden defects grow over time under cyclic loading, they reduce both structural stiffness and overall integrity. For this reason, real-time structural health monitoring (SHM) systems are essential in identifying damage before critical failure occurs [17].

In most composite structures, SHM is achieved by embedding sensors such as piezoelectric elements or fibre optic cables. However, these sensors often lack the capability to detect damage deep within the core. In foam-core composites, carbon Z-pins can be embedded in the core. When cracks develop or compression occurs, changes in electrical resistance across the pins can be measured, enabling real-time assessment of structural integrity [25]. Another approach involves stitching the foam core with a carbon fibre grid and incorporating CNT-modified glass fibre face sheets. When damage is present, the conductive network between the carbon fibres and CNTs is disrupted, leading to increased electrical resistance and signalling structural degradation [26].

However, these monitoring strategies are generally not applicable to honeycomb core structures due to geometric constraints and the difficulty of integrating conductive pathways into their open-cell architecture. Therefore, there is a growing need to develop new SHM approaches that are specifically adapted to the unique structure and limitations of honeycomb cores.

1.3. Structural Health Monitoring (SHM)

Structural Health Monitoring (SHM) is a non-invasive method used to continuously or periodically monitor the condition of a structure. The primary goal of SHM is to provide real-time information about the structural state that enables early detection of potential damage [27]. Figure 9 illustrates the SHM process, which consists of multiple stages. It begins with sensors embedded in the structure that collect critical data on factors such as vibration, strain, and temperature. These sensors continuously monitor structural behaviour and detect any deviations from normal operating conditions. The information is then sent to a data acquisition system, which gathers and records the data for further analysis. The next stage involves data management, where the information is processed and organised for efficient use in structural assessments. The final step is data analysis and diagnosis, where the information is examined to detect any structural issues. This includes identifying potential damage, updating structural models, assessing the condition of the structure, and predicting its remaining service life [28].

The aim of SHM is not only to detect structural failure but also to identify physical damage at the earliest possible stage. This allows to immediately take actions before structural failure. In doing so, this method enhances safety, extends the lifespan of structures, and optimises maintenance time and costs. The successful adoption of SHM will shift maintenance practices from conventional schedule-driven inspections to condition-based maintenance, this will improve operational safety and reduce life-cycle costs [27].

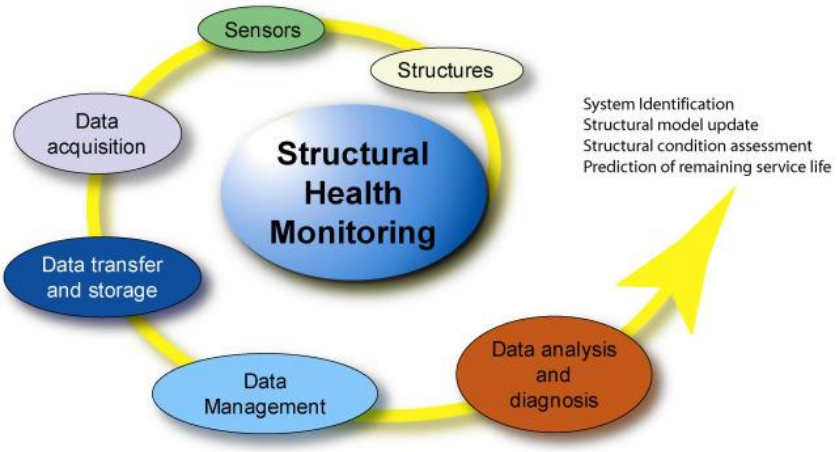

Fig. 9. Structural health monitoring concept [28]

There are two types of SHM: passive sensing and active sensing. Passive sensing SHM relies on accelerometers, piezoelectric sensors, and fibre optics to monitor structural conditions. Changes in sensor measurements occur due to external loads, damage, or environmental factors such as temperature or humidity.

Figure 10 illustrates how passive sensing SHM detects damage using piezoelectric transducers. When an impact occurs, stress waves propagate through the structure. These waves are captured by piezoelectric transducers, which convert them into electrical signals. The data acquisition system then records and analyses these signals. The graph on the right shows that when damage occurs, the signal amplitude increases, indicating an event in the structure [28].

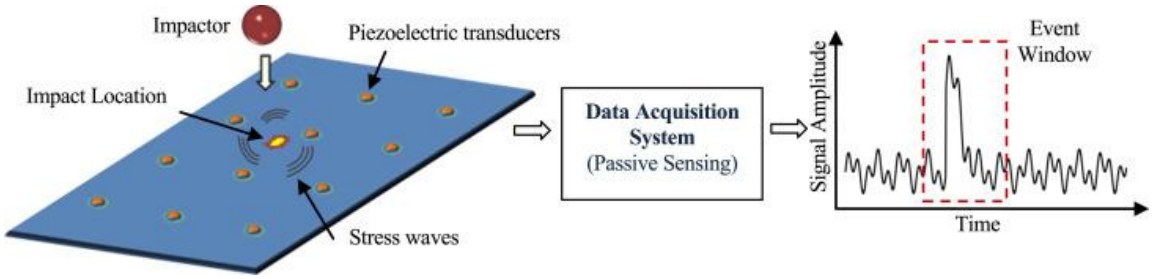

Fig. 10. Passive sensing SHM [28]

One of the key advantages of passive sensing is that it does not require additional actuators, as it relies solely on ambient vibrations and operational loads. This makes it a cost-effective method for monitoring structural health. Advanced passive sensing techniques can provide global structural information, helping to identify the presence, approximate location, and severity of damage. However, while passive sensing is effective for detecting local failures, accurately pinpointing the exact location of damage can be challenging. To improve detection reliability, sensors typically need to be placed near potential failure points [28].

In an active sensing system, transducers function both as sensors and actuators. This system uses piezoelectric sensors-actuators, which can act both as transmitters and receivers. As shown in figure 11, defects are detected by injecting controlled diagnostic signals (Lamb waves) into the structure. If the structure is undamaged, these waves travel smoothly through the material. However, when damage occurs, the waves scatter, reflect, or change in velocity and amplitude, altering the received signal. Once damage appears, local sensor measurements differ from the initial input signals. As

illustrated in Figure 11, the graph shows a clear difference between the pristine (blue) and damaged (red) signals, indicating structural damage. After detecting damage, the next step is to determine its location. By comparing the time differences of wave arrivals at different sensors (at least three sensors are needed), the exact location of the damage can be estimated [28].

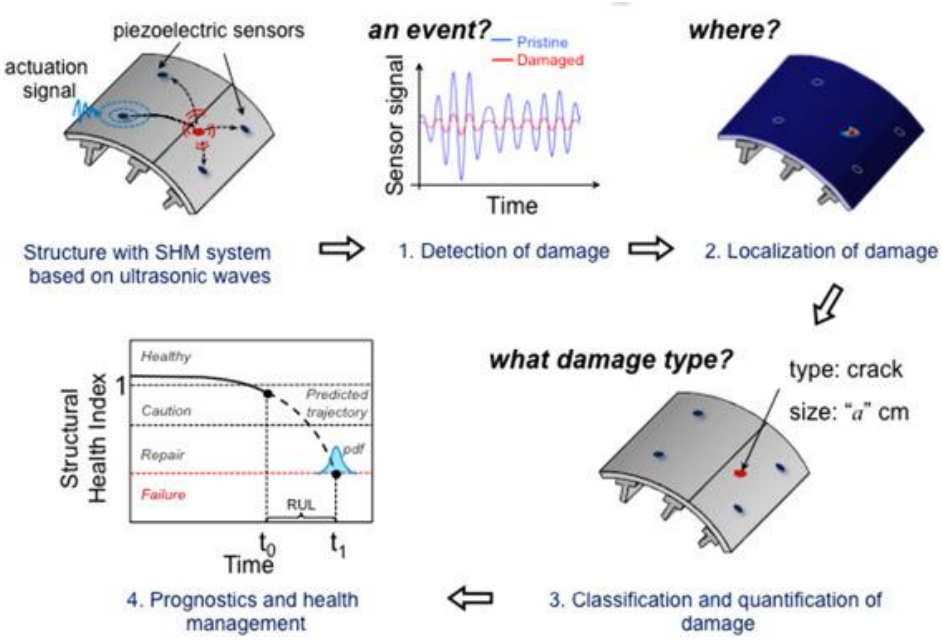

Fig. 11. Active sensing SHM [28]

While this method is highly effective, it often requires additional hardware and a power supply to operate the system. Furthermore, installing sensor networks across an entire structure may not always be feasible, so SHM is typically applied to critical hot-spot areas where damage is most likely to occur [28].

1.4. SHM sensors

As previously mentioned, SHM systems utilise accelerometers, piezoelectric sensors, or fibre optics to monitor structural conditions. These sensors must meet specific performance requirements, including the ability to detect only actual structural damage while remaining unaffected by environmental variations. Additionally, they should transmit acquired signals reliably, minimise any negative impact on the host structure, and be easy to install, integrate, and operate. For aerospace applications, sensors should also possess small dimensions, lightweight construction, durability against aging, resistance to noise, and low power consumption. Moreover, they should feature compact wiring or wireless capabilities while maintaining cost-effectiveness [29].

1.4.1. Fibre optics

Optical fibres are composed of a silica core at the centre, surrounded by a silica cladding and a polymer coating for protection. The core is the central region where light travels, designed with a high refractive index to keep the light contained inside. Depending on the core diameter, optical fibres can be single-mode or multimode. Single-mode fibres have a core diameter of approximately 10 µm and carry only one light mode, which results in higher accuracy and sensitivity. In contrast, multimode fibres have a wider core diameter of about 50–100 µm and can carry multiple light modes, allowing for longer sensing ranges but with lower accuracy and requiring higher light intensity.

The cladding surrounds the core and has a lower refractive index, ensuring total internal reflection, which keeps the light signals trapped inside. The outer polymer coating serves as a protective layer, shielding the fibre from physical damage and environmental effects. Any damage to the fibre optic structure can be detected by observing changes in its optical properties, such as intensity, wavelength, and phase of polarisation [29].

The aerospace industry favours fibre optics due to their ability to be embedded in composite materials. Their tiny size and lightweight nature make them ideal for integration into aircraft structures such as wings, stringers, cockpits, landing gear, and fuselage. These sensors provide high resolution and bandwidth for precise measurements, immunity to electromagnetic interference, simple instrumentation and multiplexing, which reduces wiring complexity, and the ability to monitor difficult-to-reach components, such as engines and structural hot spots [30].

Figure 12 presents an example of an SHM system in an aircraft utilising fibre optics. Sensors are integrated into critical aircraft structures to monitor strain, temperature, and pressure. Damage is detected by analysing changes in the reflected light spectrum. When the aircraft undergoes stress or temperature fluctuations, the wavelength of the reflected light shifts, corresponding to the intensity of the change. The interrogator unit collects the reflected light and analyses the spectral shifts, allowing the system to determine the structural condition in real time [30].

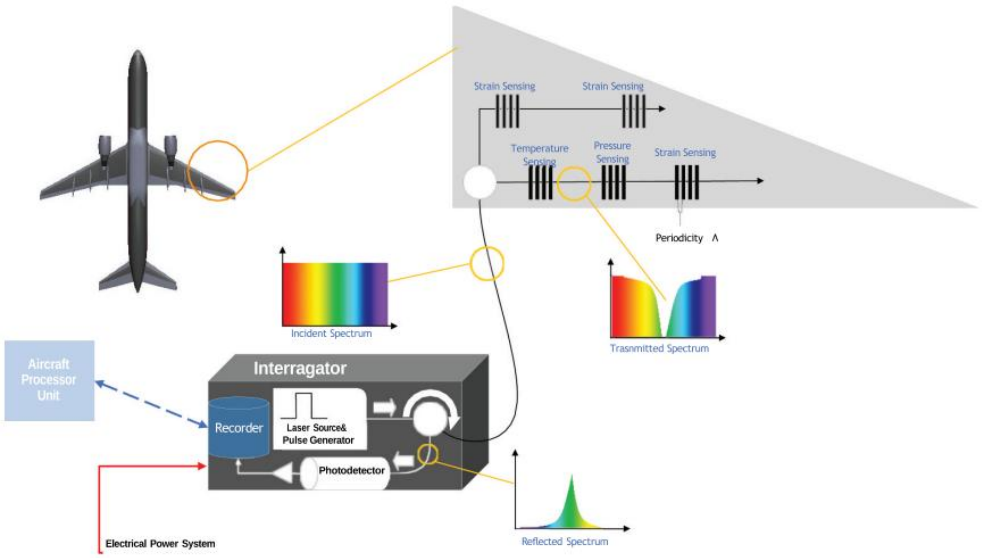

Fig. 12. Aircraft fibre optics scheme [30]

Despite the good application of fibre optics in aerospace, they also have some limitations. One of the biggest challenges is their sensitivity to temperature changes, which can affect measurement accuracy. Moreover, their installation is more complex compared to traditional sensors, requiring precise bonding techniques. While the fibres themselves are lightweight, the necessary interrogation units and processing hardware add extra weight, which is not ideal for aircraft applications. Lastly, their high costs and the need for specialised equipment make them a more expensive alternative to traditional sensors [31].

1.4.2. Piezoelectric sensors

Piezoelectric sensors convert mechanical stress into electrical voltage by relying on the piezoelectric effect. These sensors are made of piezoelectric materials that generate an electrical charge when subjected to mechanical force, strain, or pressure. This results in an electric potential difference (voltage) on the sensor's surface. The generated charge is then converted into a measurable voltage or current, which can be analysed as an electrical signal. The magnitude of the voltage is proportional to the applied mechanical stress. Damage detection is based on monitoring changes in the electrical signal of the sensor. In a healthy structure, the electrical response remains stable, whereas in a damaged structure, such as one with cracks, delamination, or corrosion, the mechanical properties change, altering the sensor's impedance or voltage output. By comparing the sensor's signal before and after stress, structural damage can be identified [32].

These sensors offer high sensitivity and can detect even minor variations in mechanical stress. Their compact and lightweight design makes them suitable for space-limited applications, while their durability allows them to withstand harsh environments. They also have a fast response time, making them ideal for real-time monitoring. However, their performance can be affected by humidity and extreme temperatures, which may lead to inaccuracies. Additionally, high-performance piezoelectric materials can be expensive, and the sensors require careful tuning and baseline measurements to ensure accurate damage detection [30].

1.4.3. Accelerometers

Accelerometers measure how structures vibrate over time. When a structure is in good condition, it vibrates in a predictable pattern, but when damage occurs, such as cracks, loosening or impact, the vibration pattern changes. By analysing these changes, accelerometers can help detect structural defects [30].

There are two main types of accelerometers: capacitive and piezoresistive. Capacitive accelerometers work by detecting changes in capacitance. Inside the sensor, there are two capacitor plates, with a small mass attached to one of them. When the structure moves, this mass also moves, altering the distance between the plates and changing the capacitance. This change is measured by an electrical circuit, which converts it into a readable signal [30].

On the other hand, piezoresistive accelerometers rely on changes in electrical resistance. These sensors contain a small proof mass that moves when the structure vibrates. This movement compresses a piezoelectric material, altering its electrical resistance. By analysing the resistance change, the force or displacement can be calculated [30].

These sensors have high sensitivity and can detect even small changes in vibration patterns, leading to early damage detection. Their small size and lightweight design allow them to be installed in tight spaces. Compared to other sensors, such as fibre optics, they are cost-effective. However, they are sensitive to environmental factors such as extreme temperatures, humidity, and electromagnetic interference, which can affect signal accuracy. To detect damage precisely, calibration with the measurement of an undamaged structure is needed. Additionally, accelerometers are prone to noise, which may require signal processing to filter out unwanted disturbances [30].

1.5. Smart composites materials

Fibre optics, piezoelectric sensors, and accelerometers, combined with machine learning and data analytics, have improved structural monitoring capabilities. However, they still face challenges such as measurement limitations, integration applicability, adhesion durability, and external system complexity [33]. Another type of SHM involves advanced composite materials embedded with nanoparticles, which significantly enhance the physical, mechanical, thermal, and electrical properties of composites. By incorporating electrically conductive nanoparticles into the composite structure, the material itself can function as a sensor for damage detection. The most common nanofillers used for this purpose are carbon nanotubes (CNTs), MXenes, and graphene [34].

1.5.1. Carbon nanotubes

Carbon nanotubes (CNTs) are elongated nanoparticles with nanometre-scale diameters and micrometre-scale lengths. They are formed by rolling up graphene sheets, and due to their unique geometric structure and strong carbon-carbon bonds, they exhibit exceptional mechanical, electrical, and thermal properties [35].

CNTs are categorised into two primary types: single-walled carbon nanotubes (SWCNTs) and multi-walled carbon nanotubes (MWCNTs). Figure 13 illustrates their structural formation from graphene. SWCNTs consist of a single graphene layer rolled into a cylindrical shape, with external diameters ranging from 0.4 nm to 3 nm and lengths typically between 0.5 to 50 μm. In contrast, MWCNTs are composed of multiple graphene layers, resembling graphite, with external diameters between 2 nm and 100 nm and lengths extending up to several millimetres [36,37].

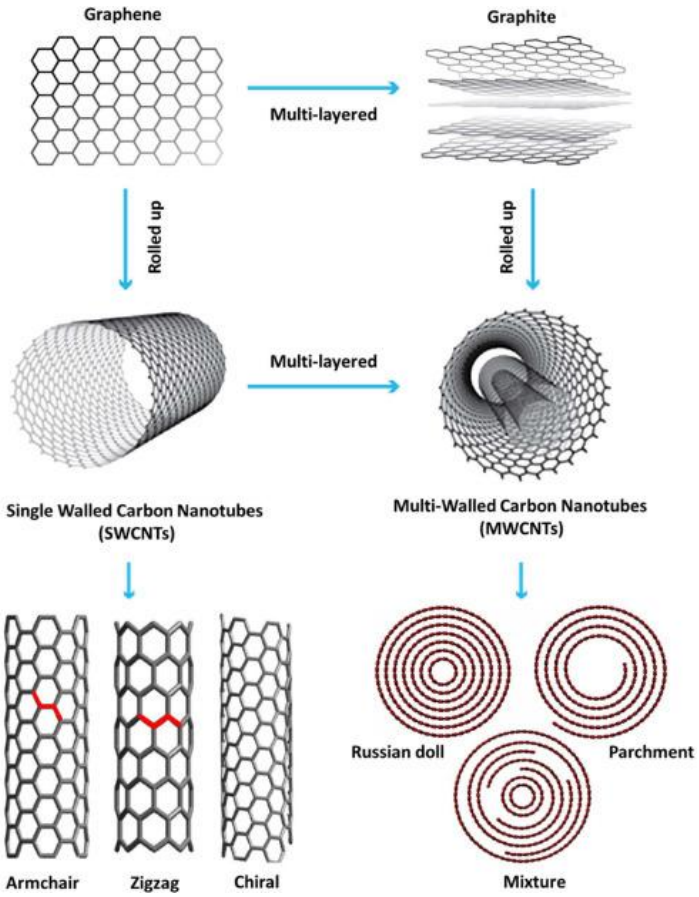

Fig. 13. Derivation of SWCNTs and MWCNTs from Graphene [35]

The small size and symmetrical structure of CNTs give them remarkable electrical properties. Their conductivity depends on how the graphene sheet is rolled. Graphene is a zero-bandgap semiconductor, meaning it does not have an energy gap between its conduction and valence bands, allowing electrons to move freely as in metals. However, when graphene is rolled into a nanotube, it can behave as either a metal or a semiconductor, depending on its chirality (n, m indices) and diameter [38].

When graphene is rolled into a nanotube, the electrons are constrained to move along the nanotube's length and around its circumference. This constraint introduces energy band folding, which determines whether the CNT behaves as a metal or a semiconductor. Additionally, the nanotube's diameter influences its bandgap: larger diameters result in smaller bandgaps due to curvature effects. For example, nanotubes around 1 nm in diameter typically have a bandgap between 0.7 eV and 0.9 eV. Moreover, the strong carbon-carbon bonding in CNTs enables them to carry high current densities, with conductivities ranging from 10^6 to 10^7 S/m [38,39].

CNTs exhibit exceptional mechanical properties due to their strong sp^2 carbon-carbon bonds. They have a high Young's modulus, outstanding tensile strength, and low density [38]. The mechanical properties of CNTs are summarised in table 2. It can be observed that multi-walled carbon nanotubes (MWCNTs) have the highest Young's modulus at 1200 GPa, making them 477% stiffer than steel, which has a Young's modulus of 208 GPa. Their tensile strength (150 GPa) is 37400% higher than steel (0.4 GPa), meaning they can withstand significantly greater stretching forces before breaking. Additionally, MWCNTs have a 67% lower density than steel (2.6 g/cm³ vs. 7.8 g/cm³), resulting in an excellent strength-to-weight ratio. When comparing MWCNTs to SWCNTs, it is evident that MWCNTs are stronger but also have a higher density [39].

Table 2. Mechanical properties of CNT [39]

	Young's modulus, GPa	**Tensile strength, GPa**	**Density, g/cm^3**
MWCNT	1200	150	2.6
SWCNT	1054	75	1.3
Graphite	350	2.5	2.6
Steel	208	0.4	7.8

These mechanical properties position CNTs highly promising for advanced applications, particularly in high-performance composites, aerospace structures, and lightweight materials where strength and low weight are critical [38].

However, the dispersion of CNTs is a major challenge due to their tendency to agglomerate. This occurs because CNTs naturally attract each other, forming clumps, and their long, thin structure makes achieving uniform distribution difficult. If CNTs are not evenly dispersed, their electrical conductivity, mechanical reinforcement, and sensing capabilities are significantly reduced. Poor dispersion leads to inhomogeneous conductive networks, diminishing the composite's self-sensing ability.

1.5.2. Carbon nanotubes in SHM

Carbon nanotubes (CNTs) have emerged as a promising material for SHM due to their outstanding mechanical, electrical, and sensing properties. Their integration into composite structures enables

real-time monitoring of infrastructure integrity through electrical resistance changes in response to mechanical stress. When pressure is applied, CNTs move closer together, enhancing conductivity and reducing resistance. Conversely, crack formation disrupts the conductive network, leading to a measurable increase in resistance [40,41].

The electrical conductivity of CNT-enhanced materials is governed by two main mechanisms: direct contact between CNTs and quantum electron tunnelling. In a well-dispersed CNT network, conduction occurs both through physical connections and tunnelling across nanometre-scale gaps. This self-sensing capability is based on the piezoresistive effect, where mechanical strain alters the material's electrical resistance, making CNT-reinforced composites highly effective for SHM applications [42].

1.5.3. MXenes

MXenes are a relatively new group of 2D nanomaterials with atomic-scale thickness and high aspect ratios. Their general formula is $M_{n+1}X_nA_x$, where M represents transition metals such as Sc, Ti, Y, Hf, V, Nb, and Mo, X is carbon and/or nitrogen, and A is an active terminal group derived from elements of groups 13 or 14 (Fig. 14). In some cases, MXenes include termination groups denoted as T_x, which may consist of -OH, -F, =O, or -Cl. Due to the wide variety of available M, X, and A elements, more than 150 different MXene compositions have been identified so far [43,44].

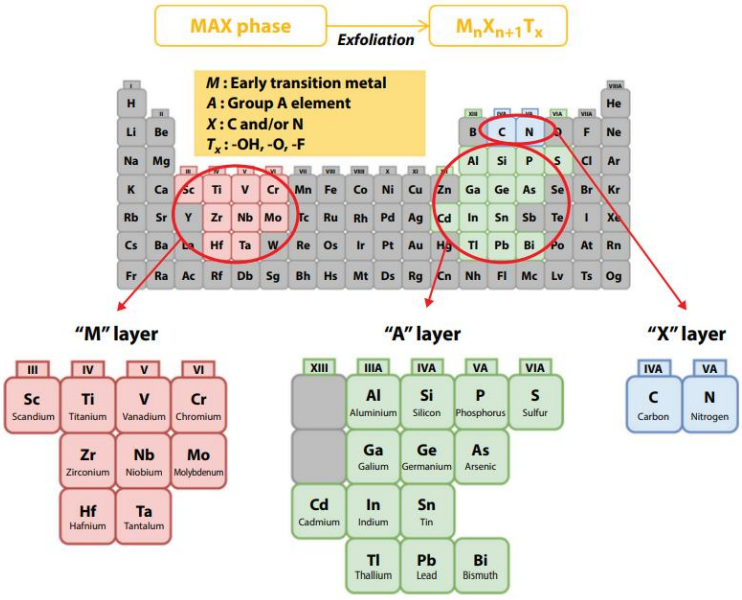

Fig. 14. Composition of MXenes [45]

MXenes are produced through a selective etching and exfoliation process, which involves the removal of A elements from the MAX phase, a process that is illustrated in Figure 15. During synthesis, hydrofluoric acid (HF) is commonly used to selectively remove the A-layer, leading to the formation of exfoliated MXene sheets. The etching process disrupts the bonding between layers, reducing their structural integrity. However, after etching, the M and X layers remain stacked together. To separate these layers into individual nanosheets, sonication is applied, producing two-dimensional MXene flakes [46,47].

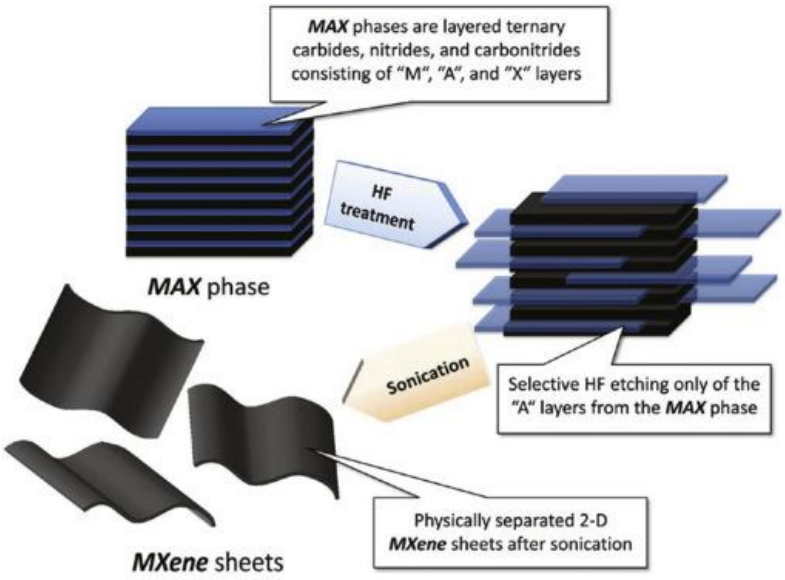

Fig. 15. Synthesis of MXenes [47]

MXene flakes have lateral sizes of up to approximately 10 μm and thicknesses ranging from a few nanometres to several micrometres. Their thickness is influenced by several factors, including the structure of the parent MAX phase, etching conditions, and post-processing modifications. The number of layers in MXenes depends on their chemical formula $M_{n+1}X_nA_x$. For instance, M_2X results in three atomic layers, M_3X_2 consists of five atomic layers, and M_4X_3 forms seven atomic layers. The structural characteristics of these materials dictate their thickness. Additionally, the etching method significantly affects both the thickness and the quality of the MXenes produced. Strong acids, such as hydrofluoric acid, tend to yield multilayered MXenes, whereas milder etching techniques allow for better control over thickness and structural integrity. To further reduce thickness, delamination techniques such as sonication and chemical intercalation are employed. Sonication utilises high-frequency sound waves to break apart MXene layers. Ultrasonic waves generate rapid vibrations and microscopic bubbles, which contribute to the separation of layers in solution. This method can produce few-layer or even single-layer MXenes, but the duration and intensity of sonication must be carefully controlled to prevent structural damage. Chemical intercalation involves the introduction of chemicals such as tetrabutylammonium hydroxide, hydrazine, or lithium ions to expand the interlayer spacing, facilitating easier exfoliation. These two methods can be used simultaneously to optimise exfoliation efficiency [47].

MXenes exhibit excellent electrical, magnetic, mechanical, and thermal properties, making them highly valuable in sensor applications. Most MXenes are metallic or semi-metallic, allowing for high electrical conductivity. Their electronic structure is determined by the combination of metal (M) and carbon/nitrogen (X) elements, as well as surface terminations such as fluorine, oxygen, and hydroxyl groups. Metallic bonding between transition metal atoms ensures efficient electron transport across the material. Table 3 presents a comparison of electrical conductivity among various MXenes and other materials. $Ti_3C_2T_x$ MXene demonstrates the highest conductivity, ranging from 5000 to 15000 S/cm, indicating its superior ability to transport charge with minimal resistance. Carbon nanotubes also display high conductivity, reaching 10000 S/cm, which is approximately ten times greater than that of other MXenes such as Ti_2CT_x, V_2CT_x, and $Nb_4C_3T_x$ [45,48].

Table 3. MXenes conductivity [45]

Material	$Ti_3C_2T_x$	Ti_2CT_x	V_2CT_x	$Nb_4C_3T_x$	Graphene	CNT	Copper
Conductivity, S/cm	5000 – 15000	1000	1000	1024	2000	10000	5960

MXenes inherit their mechanical properties from their parent MAX phase, which combines the toughness of metals with the rigidity of ceramics. When incorporated into different polymer matrices, MXenes can enhance tensile strength, impact resistance, flexibility, and wear resistance. Figure 16 illustrates the changes in the mechanical properties of composites when Ti_3CN MXene is introduced into the structure. The stress-strain graph in Figure 16a demonstrates how MXene concentration influences composite strength and strain. The black curve, representing pure polyurethane (PU), exhibits the lowest tensile strength of 14 MPa and strain at break. As MXene concentration increases from 0.125 to 0.5 wt.%, the composite becomes stronger, with the highest tensile strength of approximately 20 MPa observed at 0.5 wt.% MXene. However, when the concentration is further increased to 1.0 wt.%, the maximum tensile strength decreases due to MXene aggregation, which reduces the efficiency of load transfer within the composite [49].

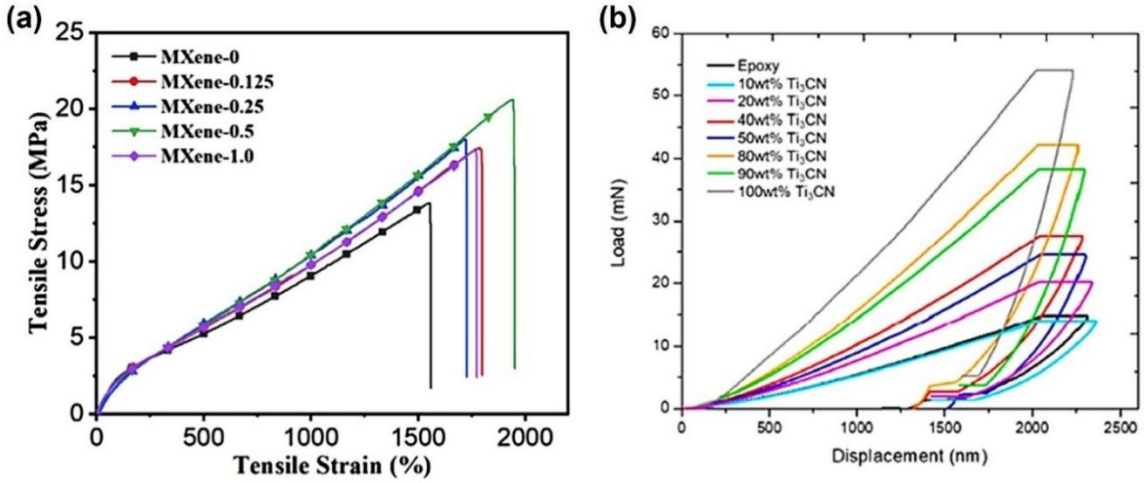

Fig. 16. Mechanical properties of Ti_3CN/epoxy composites: (a) stress–strain, (b) load–displacement [49]

The load-displacement graph in Figure 16b shows how the mechanical response changes as Ti_3CN concentration increases. Composites containing pure epoxy exhibit the highest load-bearing capacity before failure but have the lowest displacement, indicating limited flexibility. As the MXene concentration increases, the maximum load decreases, but the displacement at failure increases, suggesting improved flexibility. The concentration of MXenes within the composite plays a crucial role in either enhancing or reducing mechanical properties, depending on the dispersion and interactions of MXene within the polymer matrix [49].

1.5.4. MXenes in SHM

Due to their physical properties and chemical stability, MXenes can be used as sensing elements for quasi-static and dynamic loading. MXene-based strain sensing is enabled by the engagement and disengagement of contact between nanosheets during deformation. When an impact force is applied to the structure, cracks appear between MXene nanosheets, causing changes in electrical resistance. The increase in strain is proportional to the change in resistance. Incorporating MXenes into a

composite structure enables real-time detection of damage, including microcracks. This behaviour allows continuous monitoring of various types of defects using resistance mapping techniques [50].

MXene-based strain sensors outperform other sensing materials, such as graphene and CNTs, in terms of gauge factor, flexibility, and conductivity. Carbon-based materials suffer from lower strain sensitivity and slower response times. Meanwhile, MXene-based sensors demonstrate a higher gauge factor, allowing them to detect even minor defects. On the other hand, CNTs are more effective for large-area strain sensing due to their ability to form conductive networks within composite materials. Additionally, CNTs offer advantages in terms of lower manufacturing costs, faster production, and easier integration into composite structures. A comparison of MXenes and CNTs for damage detection in SHM is shown in table 4 [50,51].

Table 4. Comparison of MXenes and CNTs in SHM [51]

Property	**MXenes ($Ti_3C_2T_x$)**	**CNTs**
Conductivity, S/cm	5000-15000	~10,000
Gauge Factor	80-7400	~6.4
Flexibility	High	Very High
Sensitivity to Strain	Excellent	Moderate
Impact & Fatigue Sensing	Effective	Highly Effective
Embedding in Composites	Easy (good polymer interaction)	Moderate (requires dispersion control)
Manufacturing Scalability	Moderate (vacuum filtration, dip coating)	High (spray coating, CVD)

Overall, both MXenes and CNTs exhibit high damage sensitivity due to the piezoresistive effect. Their integration into the sensor sector can enhance structural safety, extend the lifespan of materials, and reduce maintenance time [51].

1.6. Summary of literature review

Nowadays, UAVs are increasingly adopted across various industries such as agriculture, construction, photography, logistics, and the military. They are particularly suitable for missions that are dangerous, repetitive, or difficult for humans to perform. UAVs can be classified into three main types: rotary-wing, fixed-wing, and hybrid drones. Rotary-wing UAVs offer excellent manoeuvrability and vertical take-off and landing (VTOL), making them ideal for short-range applications such as inspection, cinematography, and precision farming. Fixed-wing UAVs are more efficient for long-duration, long-distance missions such as mapping, surveillance, and reconnaissance. Hybrid UAVs combine the advantages of both, allowing vertical take-off along with energy-efficient horizontal flight, and are therefore suitable for diverse and flexible operations.

To meet the demands of flight, UAV structures must withstand significant aerodynamic loads while remaining lightweight. This has led to the widespread use of composite materials, which offer high strength-to-weight ratios. In particular, UAV wings are often constructed using sandwich-structured composites due to their superior bending stiffness. These structures typically consist of two thin face sheets bonded to a thicker lightweight core. The face sheets bear tensile and compressive loads, while the core resists shear and helps distribute bending stresses. One of the most used core materials in aerospace applications is aramid honeycomb, which is lightweight and has high stiffness. However,

its hexagonal cell structure results in a limited bonding area with the face sheets and renders it susceptible to moisture absorption, crushing, and wrinkling under impact. If damage remains undetected, especially under cyclic loading, it can propagate and lead to face sheet buckling, core collapse, and delamination – ultimately compromising structural integrity.

Early detection of such damage is critical. Structural health monitoring (SHM) technologies such as strain gauges, piezoelectric transducers, fibre optics, and accelerometers are commonly used for real-time damage tracking. However, these systems face limitations: they often require complex installation, additional power sources, and may not effectively capture internal or subsurface damage in composite or honeycomb cores. Furthermore, traditional sensors may degrade over time or lose effectiveness in harsh environmental conditions.

To overcome these challenges, smart composites with embedded nanomaterials have emerged as a promising solution. By integrating electrically conductive nanoparticles such as carbon nanotubes (CNTs) and MXenes into the composite structure, the material itself becomes capable of damage sensing. These nanomaterials form conductive networks that respond to mechanical stress or damage by altering electrical resistance. This piezoresistive behaviour enables continuous, distributed sensing throughout the structure without the need for bulky external sensors.

The goal of this research is to develop an advanced sandwich-structured incorporating CNT and MXene particles for real-time damage detection and localisation in UAVs. This approach aims to improve structural reliability, enable proactive maintenance, extend the operational lifespan of UAVs, and enhance mission safety in demanding environments.

2. Materials and methods

2.1. Materials

In this work, MXene and CNT nanoparticles were used to enhance the electrical conductivity of the composite.

2.1.1. Honeycomb dip-coated MXenes

To fabricate a conductive honeycomb core, Ti_3C_2Tz MXenes were synthesised from Ti_3AlC_2 MAX phase with a particle size of less than 40 µm and a purity of 98 wt.%. The etching process employed a mixture of hydrochloric acid (HCl) and lithium fluoride (LiF), which generated hydrogen fluoride (HF) in situ to selectively remove the Al layer from the MAX phase. The MAX powder was gradually introduced into the etching solution and stirred continuously for 24 hours to ensure complete reaction.

After etching, multilayer MXenes were delaminated using 99 wt.% lithium chloride (LiCl). The resulting suspension underwent centrifugation twelve times at 3500 rpm and was repeatedly washed until the supernatant achieved a pH higher than 6, ensuring minimal acidic residues. The final concentration of delaminated MXenes in the supernatant was approximately 3.3 mg/mL.

To increase the concentration of MXenes, a rotary evaporator was used (Fig. 17). During this process, the suspension was placed in a rotating flask (containing the black MXene supernatant) and spun at 90 RPM. The flask was partially submerged in a water bath heated to 63 °C. Simultaneously, a vacuum pump was used to lower the pressure, allowing the solvent to evaporate at a reduced temperature. The rotation of the flask distributed the liquid into a thin film along the inner surface, significantly enhancing the evaporation rate. The evaporated solvent was condensed in a water-cooled condenser and collected in a receiving flask. This process left behind a concentrated MXene solution, which after 120 minutes reached a final concentration of 0.54 mg/mL.

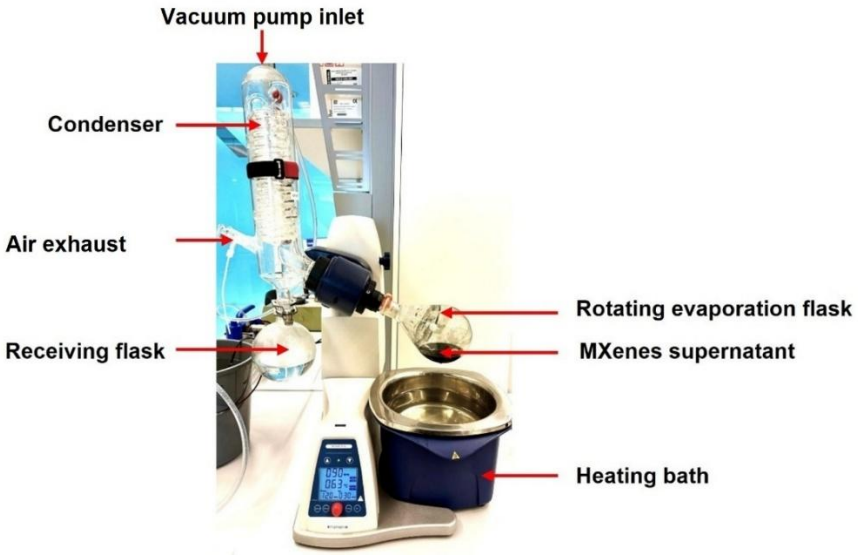

Fig. 17. Rotary evaporator setup for concentration of MXene supernatant

To impart conductivity, a 5 mm thick aramid honeycomb core with dimensions of 10 × 10 cm was dip-coated in the prepared MXene solution (Fig. 18a). The honeycomb was subjected to up to three consecutive dip-coating cycles. After each cycle, the sample was dried in an oven at 100 °C for 10 minutes, and the overall electrical resistance of the honeycomb was measured. After the first dip, the

resistance was approximately 10.5 kΩ. Following the second dip, resistance dropped to around 0.7 kΩ (a 93% reduction), and after the third dip, it was further reduced by approximately 50% (Fig. 18b). These results confirmed the successful tuning of conductivity through multiple coating cycles.

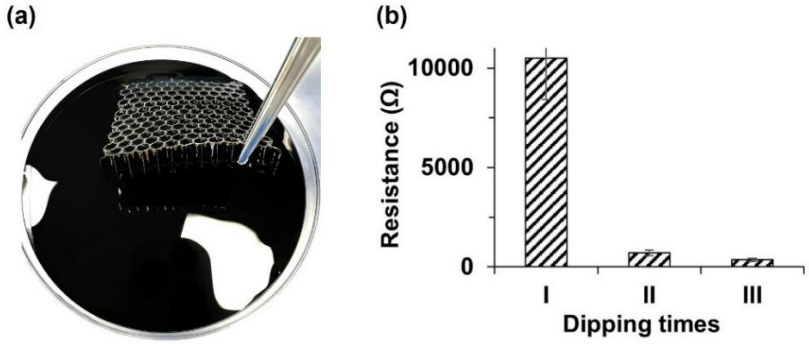

Fig. 18. (a) – honeycomb dip-coating in MXene water solution; (b) – resistance dependence on the number of dipping times

To evaluate the spatial distribution of conductivity, a separate 6 × 6 cm aramid honeycomb sample was dip-coated twice in the same MXene solution. After drying, the sample was cut into 1 × 1 cm² segments. The resistance of each individual square was measured to assess uniformity across the honeycomb surface. This evaluation ensured consistent performance and verified the effectiveness of the dip-coating process. For final composite fabrication, the honeycomb was coated twice.

2.1.2. Glass fibre spray-coated CNT

To prepare conductive glass fibre layers, a PEDOT/(CNT+SO_3H) aqueous paste was diluted with distilled water in a 1:1 ratio and subsequently reconcentrated to 0.35 mg/mL to improve sprayability. The dispersion was homogenised using a vibrating ultrasonic probe, which provided localised ultrasonic energy and helped reduce CNT agglomeration by enhancing dispersion.

A 10 × 10 cm glass fibre (GF) fabric was used for preliminary spray-coating trials (Fig. 19a). The fabric was spray-coated with the prepared PEDOT-CNT solution and dried in an oven at 100 °C for 10 minutes after each of the three coating cycles. After the first spray, the resistance was measured to be approximately 80 kΩ. Following the second spray, resistance decreased to approximately 15 kΩ. After a third spray, it further dropped to around 7 kΩ, demonstrating improved conductive coverage with each layer (Fig. 19b).

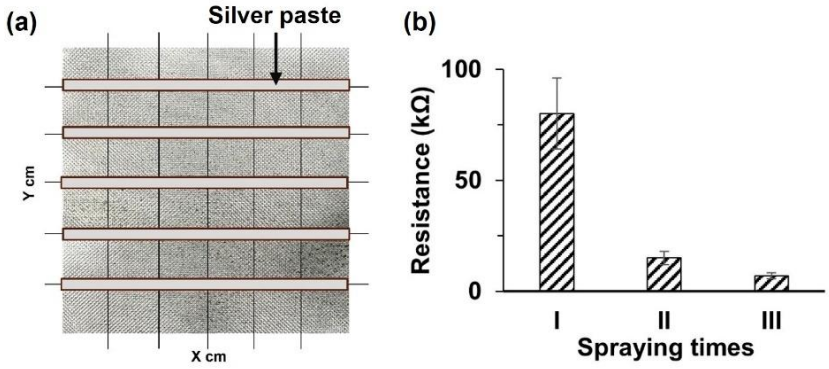

Fig. 19. (a) – GF spray-coated with CNT; (b) – resistance dependence on the number of spray coatings

To assess the coating uniformity, a second 6 × 6 cm GF sample was prepared and spray-coated twice using the same PEDOT-CNT solution. This sample was then cut into 1 cm wide stripes, and each stripe was segmented into 1 × 1 cm^2 pieces. Silver paste was applied to two opposite edges of each square in the X-direction (Fig. 19a) to serve as electrical contacts. Resistance was measured individually for each segment, allowing evaluation of coating consistency across the surface. For the fabrication of the final sandwich composite, the GF was spray-coated twice.

2.1.3. Scanning electron microscopy

The morphologies of the MAX phase, MXenes, and PEDOT-CNT were examined using scanning electron microscopy (SEM). The analyses were performed with a ZEISS EVO 40HV microscope. Samples, including the honeycomb dip-coated in a water-based MXenes solution and the glass fibre spray-coated with PEDOT-CNT, were carefully prepared and scanned to observe their structural characteristics.

2.1.4. Composite structure

A sandwich-structured glass fibre-reinforced polymer (GFRP) composite was created with three layers, each having different electrical conductivities. The composite model is shown in Fig. 20. The top interlayer is glass fibre (GF), with one side spray-coated with PEDOT-CNTs, while the other side remains non-conductive. The coated side faces the honeycomb to facilitate electrical current transfer. A 3K carbon fibre thread was manually stitched into this layer using a needle, ensuring 1 cm contact with the honeycomb for local electrical resistance measurement. The stitching was oriented perpendicularly to the unidirectional carbon fibre (UCF) layer. The middle layer consists of a conductive aramid honeycomb, dip-coated in an MXene water solution. The bottom interlayer is composed of UCF, which serves as a current collector. The face sheets of the composite consist of two layers of GF.

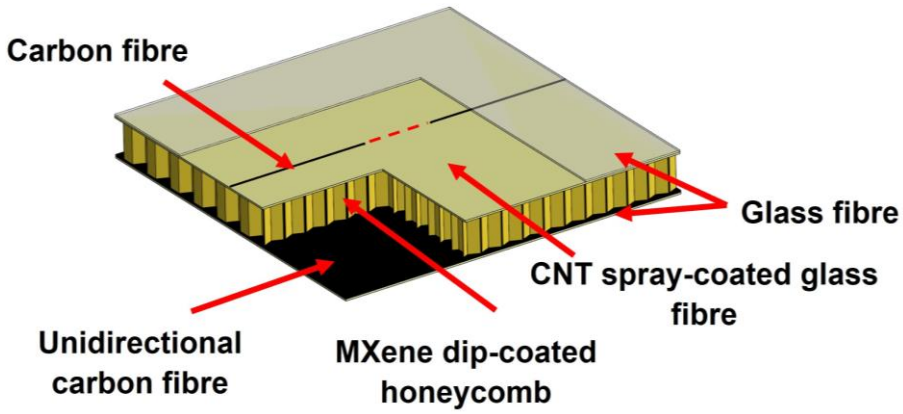

Fig. 20. Composite's model

The composites were fabricated using hand lay-up and vacuum bagging methods. The layers were bonded with a thermosetting epoxy resin (Bisphenol F-epichlorohydrin) mixed with an amine curing agent in a 10:3 ratio. After an initial curing period at room temperature for 24 hours, specimens were post-cured in a convection oven at 100 °C for four hours. To achieve specific surface textures, a peel-ply fabric (polyamide 6.6) was used for rough surfaces, while a polyethylene film created glossy surfaces.

2.2. Analytical model

As previously described, the developed self-sensing composite structure consisted of three distinct electrically conductive layers: CNT-spray-coated GF, MXene-coated aramid honeycomb, and unidirectional carbon fibre. Each layer exhibited significantly different electrical resistance values. The resistance of the UCF layer was measured to be approximately 1 Ω, the MXene-coated honeycomb exhibited the resistance of around 500 kΩ, and the PEDOT-CNT spray-coated GF layer showed the resistance of approximately 10 kΩ. Due to these considerable differences in conductivity, electrical current preferentially flowed through the path of least resistance starting from the most conductive layer (GF coated with PEDOT-CNT), passing through the intermediate honeycomb layer, and finally reaching the bottom UCF layer (Fig. 21).

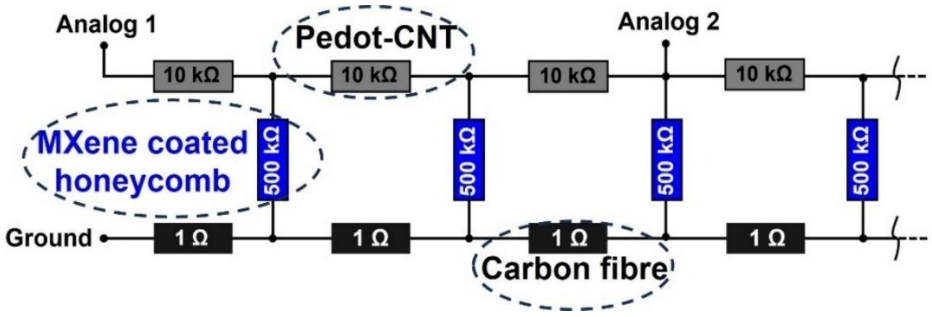

Fig. 21. Resistances of different layers

In the presence of mechanical damage, the conductive networks within the composite structure are disrupted, leading to an increase in electrical resistance. The magnitude of this increase depends on the proximity of the damage to the conductive channel: resistance increases more significantly when damage is closer to the current path and less when it is farther away. This phenomenon enables the detection and localisation of both the position and propagation of damage within the composite.

To model this behaviour, an analytical simulation was developed in "Microsoft Excel", using resistance measurements obtained from both the GF layer spray-coated with CNTs and the honeycomb dip-coated in MXene solution. Resistance data was gathered from 1 × 1 cm² surface segments of each material. These values were used to construct two separate resistance matrices corresponding to the top (CNT spray-coated GF) and middle (MXene-coated honeycomb) layers of the composite. Each matrix represented a 5 × 10 cm area, with individual nodes corresponding to measurement points across the surface.

For the honeycomb resistance matrix, values were randomised within a range of 7500 Ω to 125000 Ω, reflecting measured variations. In contrast, for the CNT spray-coated GF matrix, a constant linear resistivity of 1000 Ω/mm was assumed, and the resistance at each point was calculated based on its X-coordinate position (distance along the current path).

The total resistance at each coordinate was obtained by summing the local values from the CNT and MXene matrices. This resulted in the creation of a third matrix referred to as the bottom point current matrix. A circuit voltage of 5 V was applied, and Ohm's law was used to calculate the resulting current at each point by dividing the applied voltage by the total resistance. The current values were then summed along each vertical column, allowing a clear visualisation of current distribution across the composite surface.

To study the influence of CNT concentration on performance, the analytical model was repeated for five different CNT resistivity levels. This enabled the evaluation of current flow along the length of the composite and the identification of optimal CNT loading for maximum conductivity and sensitivity.

Furthermore, the model was designed to simulate mechanical damage by modifying the resistance of selected nodes. Damage was introduced by setting the resistance at specific points to 10^{15} Ω, effectively simulating a damaged conductive path. The approach allowed simulation of various damage types, including indentation and delamination, and the resulting current distributions were later compared with experimental results for validation. Delamination test matrix size was made 20 x 50 mm to be equivalent to the experimental sample.

2.3. Experiments

The prepared self-sensing composite was subjected to a series of mechanical and environmental tests, including three-point bending, delamination, and temperature variation tests. Additionally, localised indentation tests were conducted on individual layers to evaluate how different conductive materials respond to mechanical damage. These tests were carried out separately on three distinct configurations: a honeycomb structure dip-coated in a water-based MXene solution, a glass fibre layer spray-coated with CNTs, and the fully assembled sandwich-structured composite.

The first sample tested was a sandwich-structured composite consisting of a non-conductive aramid honeycomb core positioned between four layers of GF. Among the four GF layers, one was spray-coated with CNTs twice to impart conductivity. This conductive layer was placed such that the coated side faced the honeycomb core. The total dimensions of the sample were 100 × 50 mm. Two carbon fibre threads were integrated into the structure as sensing elements to enable real-time resistance monitoring. The sample was subjected to two consecutive indentation events at its centre: first using a 15 mm diameter spherical indenter, followed by a second indentation at the same location with a 50 mm diameter indenter to assess the response under increased compressive loading. Electrical resistance was continuously measured during the entire test using a digital multimeter (Fig. 22a).

The second tested configuration consisted of a 50 × 50 mm honeycomb structure that had been dip-coated twice in the MXene solution. To facilitate resistance measurements, aluminium foil was applied to its surface. The sample was compressed at its centre using a 15 mm spherical indenter, while changes in resistance were recorded to assess damage sensitivity (Fig. 22b).

The third sample was a complete sandwich-structured self-sensing composite, measuring 100 × 50 mm, as shown earlier in Fig. 20. This composite included two embedded monitoring channels, labelled A and B. Localised damage was introduced by applying compressive force using a 15 mm diameter spherical indenter at intervals of 2 cm along the length of the sample, progressing from channel A to channel B. Each indentation was approximately 4 mm deep. Following each indentation, the resistance was measured in both channels to assess the impact of localised damage on the composite's electrical behaviour (Fig. 22c).

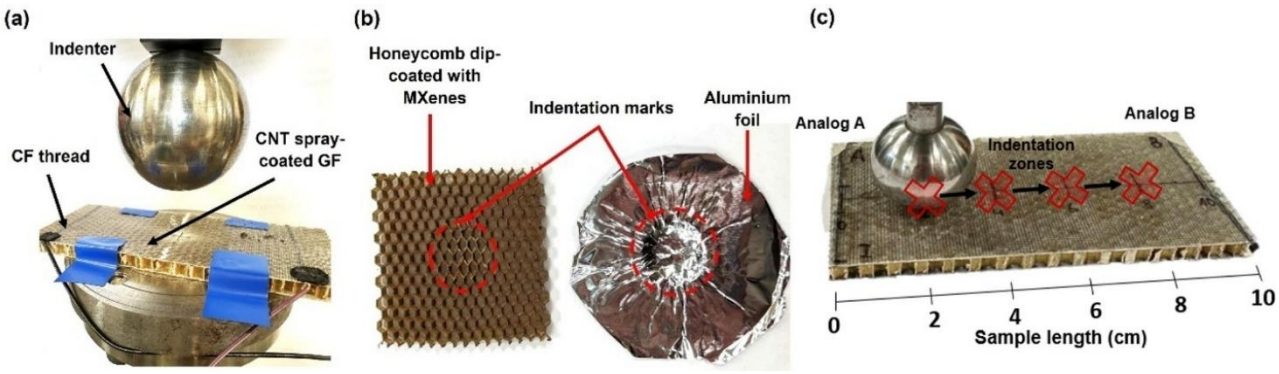

Fig. 22. Indentation test on: (a) GF spray-coated CNT; (b) honeycomb dip-coated with MXenes; (c) self-sensing composite

For the three-point bending test, a 100 × 20 mm self-sensing composite sample was prepared. The test was conducted using a Tinius Olsen H25 KT universal testing machine in accordance with the ISO 178 standard. During testing, the CNT coated GF layer was oriented upward, positioning it on the compressive side of the bending setup. The unidirectional carbon fibre (UCF) layer was located at the bottom, on the tensile side. Bending was performed at a constant crosshead speed of 2 mm/min, and electrical resistance was continuously recorded throughout the loading process to monitor the structural response (Fig. 23).

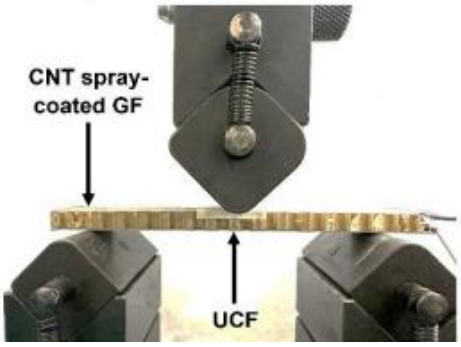

Fig. 23. Three-point bending test

The delamination test was performed in accordance with ASTM D1781, which specifies the drum peel test procedure. The purpose of this test was to monitor how electrical resistance changes as the delamination length increases between the CNT-coated glass fibre (GF) layer and the MXene-coated honeycomb core (Fig. 24). The size of the sample is 100 × 20 mm and the delamination length is 50 mm. A drum with a diameter of 5 cm was manually rolled along the surface of the sample to gradually extend the delaminated area. Although the applied force was not measured, the drum was advanced in approximately 1 cm increments, and electrical resistance was continuously recorded throughout the process. Based on the distance covered and the timing of resistance measurements, the delamination length was estimated, allowing resistance data to be correlated with the growth of the delaminated region.

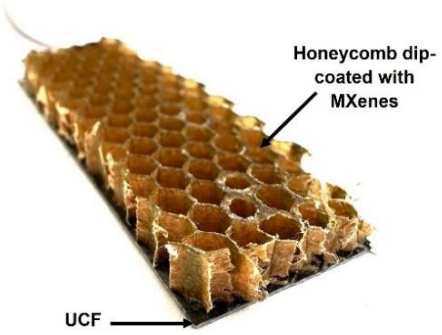

Fig. 24. Delamination test

Lastly, the composite was tested under varying temperature conditions to evaluate its electrical response in extreme environments. The samples were exposed to temperatures ranging from −14 °C to 70 °C by placing them alternately in a freezer and an oven. Electrical resistance was measured in real time at every 1 °C increment throughout the temperature change. This allowed for a detailed assessment of how thermal variations influenced the composite's conductivity and overall structural stability.

2.4. Wing section prototype

Using the developed method, a multifunctional composite wing was fabricated for structural health monitoring. The wing structure consists of four GF face sheets, a conductive honeycomb core coated with MXenes, and a UCF layer that serves as the electrical ground. Among the four GF layers, one was specially modified to act as the sensing interface by being spray-coated twice with a conductive CNT-PEDOT solution. This modified GF layer was manually stitched with six carbon fibre (CF) threads, which serve as resistive channels for damage detection. The layout of these stitched threads is shown in Figure 25.

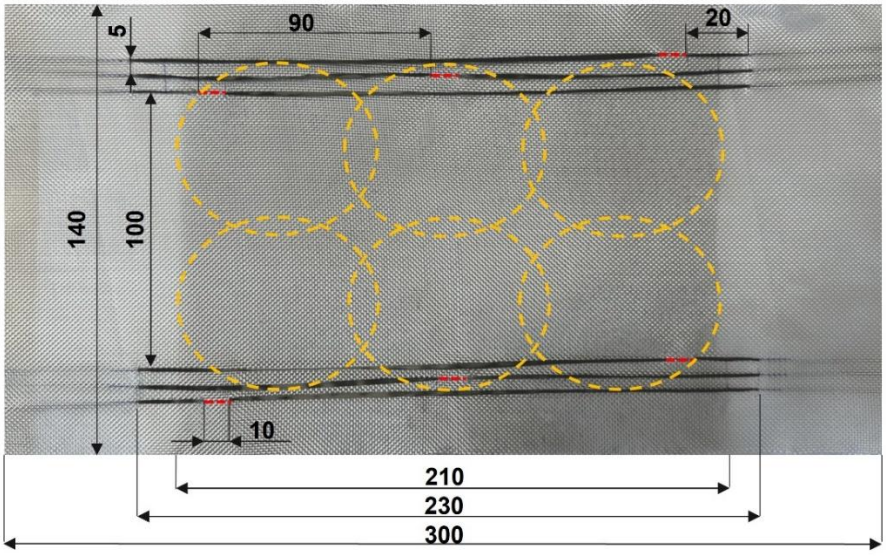

Fig. 25. Layout of carbon fibre thread sensors stitched onto a CNT-coated GF layer. Red dashed lines indicate contact zones with the honeycomb; yellow dashed lines represent overlapping sensing areas (dimensions in mm)

The CF threads were arranged in two rows – three on the top side and three on the bottom – symmetrically across the wing structure. Each CF thread overlaps with the honeycomb core by 10

mm (highlighted in red dashed lines), with a 5 mm spacing between adjacent threads. Together, these channels define six elliptical sensing zones (outlined by yellow dashed lines), which partially overlap. This overlapping design enables redundancy and damage localisation, as damage occurring in one zone can influence readings in adjacent channels, thereby allowing for more robust detection of damage growth and propagation.

It is important to note that the side shown in Figure 25 is the uncoated surface of the GF layer, which does not face or contact the honeycomb. The opposite side of this same layer coated with CNTs is the one that interfaces with the conductive honeycomb core.

To enable real-time wireless monitoring, the six CF thread channels were connected to an “Arduino Nano ESP32 Wi-Fi“ microcontroller (Figure 26). This compact device, measuring 45 × 18 mm, features 14 digital I/O pins and 8 analog input channels, making it ideal for multi-channel sensor integration. It supports both Wi-Fi and Bluetooth communication, allowing data to be transmitted wirelessly and monitored remotely. During testing, six analog channels (A0–A5) were assigned to the CF threads, and the shared UCF layer was connected to the “ESP32’s“ ground. The system was powered using a compact Li-ion battery, offering portable operation. The ESP32 supports an input voltage range of 6–21 V, which suits most small-scale battery packs [52].

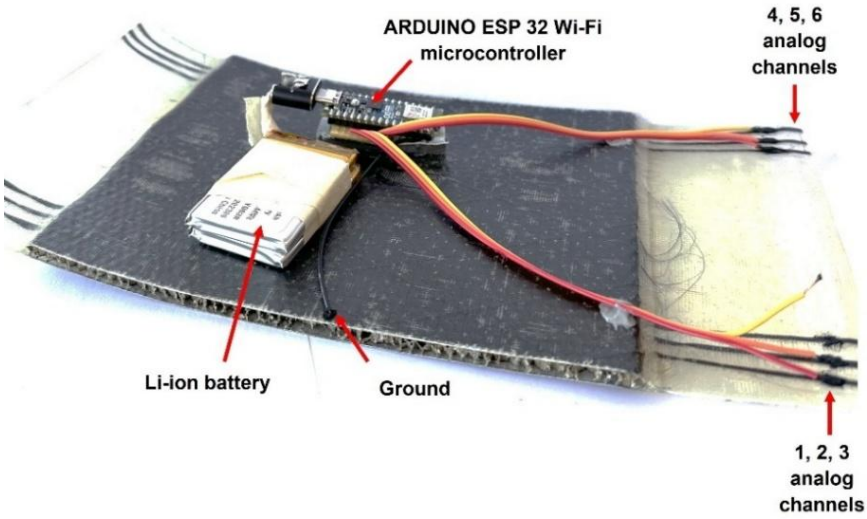

Fig. 26. Wing section prototype (top side)

The program that was used to read the resistances was written on the “Arduino Cloud“ platform, which offers wireless visualisation. The code used in this project is provided in Appendix 1. Each channel was connected in series with a known reference resistor (100 Ω), forming a voltage divider. This approach allows the microcontroller to determine the resistance of each stitched CF thread by reading voltage values and comparing them to the reference. The use of a 100 Ω resistor ensures that the system is sensitive enough to detect subtle resistance changes caused by damage, while remaining within the voltage resolution limits of the “ESP32's“ analog-to-digital converter.

The output from the composite wing is a real-time stream of resistance values from all six channels, enabling continuous structural health monitoring. These values can be visualised via the “Arduino IoT Cloud“ dashboard on a web browser or through the “Arduino IoT Remote App“ on a smartphone, allowing remote observation of structural integrity without physical inspection.

3. Results

3.1. MXenes and PEDOT-CNT characterisation (SEM)

Scanning electron microscopy (SEM) was used to examine the surface morphology of composite samples coated with PEDOT-CNT and MXene, as shown in Figure 27. PEDOT-CNT was sprayed onto the GF surface, whereas MXene was applied to the aramid-based honeycomb structure by dip-coating. The resulting micrographs illustrate how these nanomaterials adhere to different substrates and form conductive networks, which are relevant for improving functional properties and enabling structural health monitoring.

Images a, b, and c in Figure 27 depict the PEDOT-CNT distribution on glass fibre layers exposed after delamination. In the low-magnification view (Figure 27a, × 50), the woven fibre structure is clearly visible, with individual fibre bundles approximately 8 µm wide. A yellow dashed line marks the area where the honeycomb structure has delaminated. In Figure 27b (× 300 magnification), the delaminated region reveals the interface between the polymer matrix and GF, where the PEDOT-CNT coating remains attached to the fibre surface, suggesting good adhesion. At higher magnification (Figure 27c, × 10,000), a dense network of carbon nanotubes becomes evident. These nanotubes, approximately 5 µm in length, overlap to form continuous, mesh-like pathways distributed across the fibre surface. Their entanglement and coverage indicate the formation of a percolated conductive network capable of responding to mechanical deformation or damage.

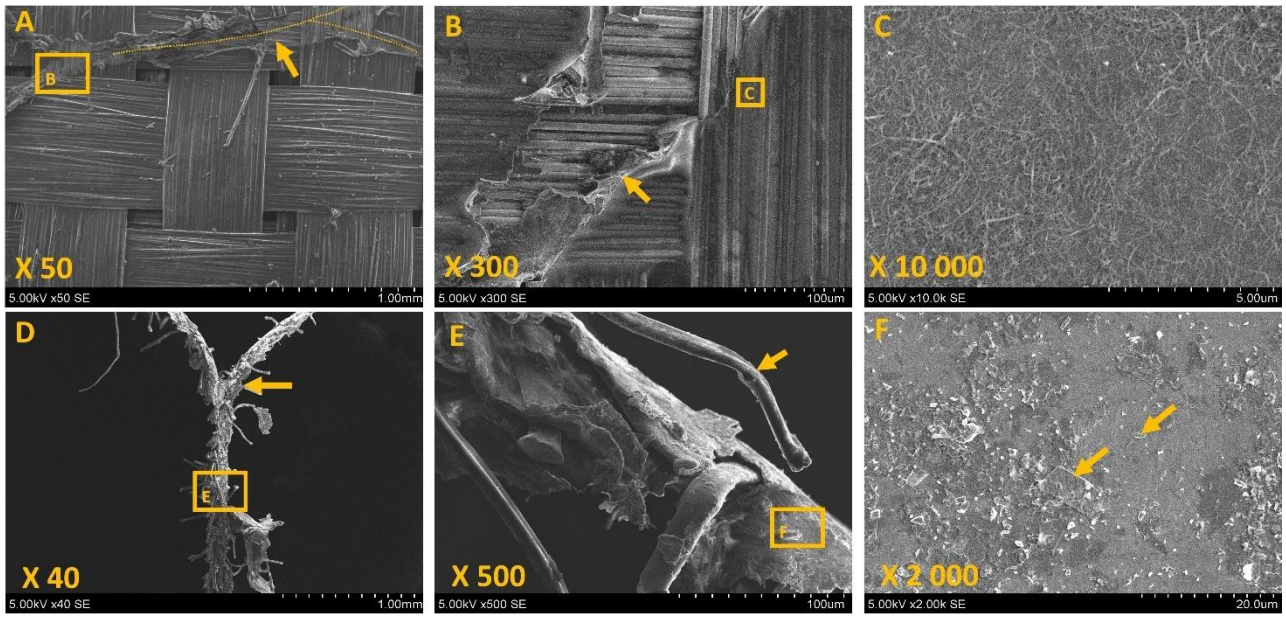

Fig. 27. SEM images of PEDOT-CNT (a, b, c) and MXenes (d, e, f)

The second set (d, e, and f in Figure 27) shows MXene flakes on the wall of the honeycomb, composed of bonded aramid sheets. In Figure 27d (× 40), the coated wall displays the fibrous, uneven surface of aramid, with visible splinters and rough microstructure. MXene particles are seen adhering to these textured surfaces. At × 500 magnification (Figure 27e), the coating conforms to the contours of the aramid fibres, forming tightly bonded regions. In Figure 27f (× 2,000), the morphology of the coating reveals flakes of varying sizes (0.5–4 µm) dispersed across the surface. The flakes overlap and stack in multiple orientations, resulting in a dense, heterogeneous layer. This structure is expected to

provide electrical conductivity while maintaining mechanical flexibility, allowing it to respond to localised strain or cracking.

Overall, the SEM observations confirm that PEDOT-CNT and MXene form stable and well-distributed coatings on GF and aramid substrates, respectively. These nanomaterials create interconnected conductive networks on otherwise insulating materials, offering not only enhanced electrical performance but also the potential for damage sensing. Their responsiveness to microstructural changes via conductivity variations makes them suitable candidates for integration into smart composite systems designed for real-time structural health monitoring.

3.2. Local areal resistance

To ensure the functionality of the self-sensing composite, it is essential to maintain uniform electrical resistance throughout the material. Consistent resistance distribution indicates homogeneous nanomaterial coverage, which is critical for reliable sensing performance. Therefore, the coating uniformity in each layer was analysed.

Figure 28a presents the local areal resistance distribution of GF fabric spray-coated with CNTs. The resistance values vary across the surface, ranging from approximately 6 kΩ/cm in the central region to a maximum of 14 kΩ/cm near the corners. This increase in the corners suggests that the CNT coating is more uniform in the middle and becomes less consistent toward the edges. This pattern may result from the nature of the hand spray-coating process, where edge effects and reduced material deposition can lead to coating inhomogeneity. Nonetheless, the central area exhibits relatively stable resistance, indicating a reasonably even CNT distribution in the most critical region for sensing applications.

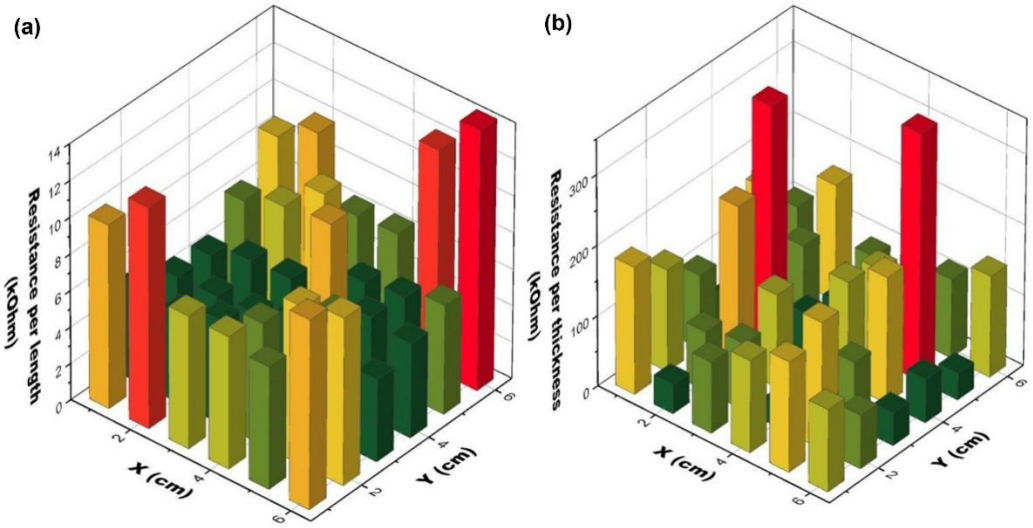

Fig. 28. Local areal resistance of: (a) GF spray-coated CNT; (b) honeycomb dip-coated with MXenes

Figure 28b shows the local resistance per thickness for a honeycomb structure that was dip-coated with MXenes. In this case, the resistance distribution is more scattered and less uniform than in the spray-coated CNT layer. The average resistance is around 150 kΩ per unit thickness, but certain areas, particularly the two red-coloured corner regions, show values as high as 280 kΩ. These highly localised peaks highlight potential coating inconsistencies during the dip-coating process, possibly due to fluid dynamics, air bubble entrapment, or inadequate MXene infiltration in those zones.

These resistance distribution patterns were taken into account when developing the analytical model for the smart composite system. However, the non-uniform coating, especially in the honeycomb core, could have contributed to the discrepancies observed between the experimental results and the analytical predictions. Ensuring more homogeneous coating coverage in future iterations may help to minimise these deviations and improve model accuracy.

3.3. Analytical model

The composite's sensing capability is primarily determined by the electrical properties of CNTs and MXenes. The analytical model was used to examine how the sensing length of the composite depends on the conductivity ratio between CNTs and MXenes. Figure 29 illustrates how the current behaves along the length of the composite. In all cases, the current gradually decreases as the sample length increases. This trend follows Ohm's law, where resistance accumulates as the electrical path extends, reducing the current flow.

When the CNT-to-MXene resistance ratio is 10:1 (black dots), the sensing length is limited to only 10 mm, meaning that any structural damage occurring beyond this point would remain undetected. As the MXene content increases and the ratio reaches 1:1 (orange crosses), the sensing length extends to around 20 mm. Further enhancement in conductivity is observed at a ratio of 1:5 (red squares), with the sensing range increasing significantly to 80 mm. A similar sensing length is maintained for the 1:10 ratio (red triangles). Finally, at a ratio of 1:20 (red circles), the sensing range spans the full length of the 100 mm sample. However, the high conductivity at this ratio reduces the resolution and sensitivity of local damage detection, making it more difficult to pinpoint the precise damage location.

These results indicate that the optimal CNT-to-MXene ratio for structural health monitoring lies between 1:5 and 1:10. This range provides a balanced trade-off between signal propagation and sensitivity, ensuring that damage is detectable over a substantial distance without compromising resolution. It is evident that sensitivity is highest near the electrical channel, with diminishing current response at further distances when the conductivity is insufficient.

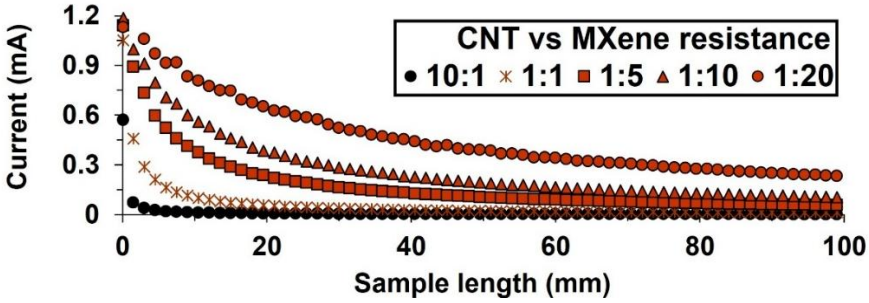

Fig. 29. Sensing length of the analytical composite model influenced by the conductivity ratio between CNTs and MXenes

To further evaluate the sensing performance of the composite, impact damage was simulated using the analytical model at a CNT-to-MXene ratio of 1:10. Figure 30 illustrates the simulation results, where damage zones are modelled as circular regions (15 mm in diameter) with significantly increased resistance, up to 10^{15} Ω, representing electrically non-conductive areas.

In Figure 30a, a single impact was introduced at the 20 mm position along the composite. At this location, the current dropped sharply from approximately 1.2 mA to 0.4 mA, indicating a clear and

localised detection of damage. The drop is nearly 2.5 times, reflecting a significant resistance increase and effective disruption of the conductive pathway. In Figure 30b, additional impact zones were introduced every 20 mm, simulating multiple damage events. As seen in the current profile, each impact location corresponds to a distinct drop in current, confirming the ability of the composite to detect multiple, spaced-out impact damages and enabling tracking of damage propagation.

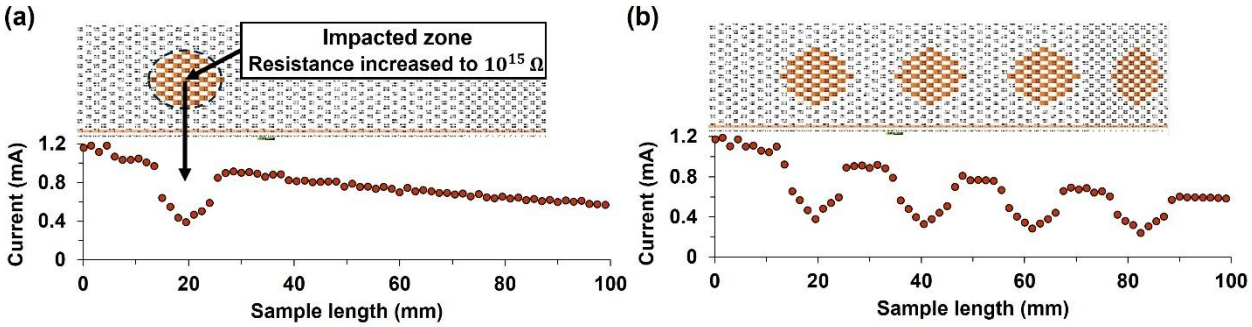

Fig. 30. Analytical composite model current drop at artificial impact zones: a – first impact at 20 mm; b – four impacts

Further analysis was carried out on a delamination scenario, using the same CNT-to-MXene ratio of 1:10 as in the impact damage simulations. In this case, a smaller matrix of 50 × 20 mm was modelled. Delamination was simulated by assigning a resistance of 10^{15} Ω to entire rows of channels, beginning from one edge and moving progressively closer to the main electrical channel. This setup imitates the gradual separation of the glass fibre layer from the honeycomb core. As shown in Figure 31, delaminating just 10 mm of the composite caused the current to drop sharply from 0.2 mA to zero. This complete loss of current indicates that when a continuous row of conductive pathways is disrupted, the electrical network becomes non-functional, entirely halting signal transmission.

Moreover, the initial current in this delamination matrix is 0.4 mA three times lower than in the matrix used for impact simulations, which reached a peak current of 1.2 mA. This discrepancy highlights the influence of sample size on baseline current. Larger matrices offer more extensive conductive paths, resulting in lower resistance and higher current flow, whereas smaller samples are inherently more resistive.

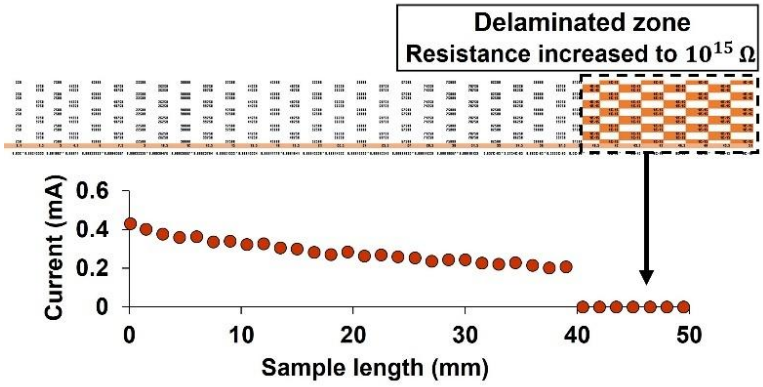

Fig. 31. Current drop after delamination

This analytical model proves to be a valuable tool for predicting the sensing behaviour of the composite. It allows for scalable simulation across various composite geometries and enables

optimisation of the CNT-to-MXene ratio for maximum sensitivity and sensing coverage. Furthermore, it provides crucial insight into how current propagates through the structure and how different types of damage, whether impact-induced or interfacial delamination, affect the electrical response. The ability to simulate damage scenarios and corresponding electrical behaviour can guide both material design and sensor placement strategies in smart composite systems.

3.4. Experimental testing

3.4.1. Indentation test

As previously discussed, understanding how different layers of the composite respond to mechanical damage is crucial for evaluating self-sensing behaviour. The first set of indentation tests was performed on a honeycomb structure dip-coated with MXenes. Figure 32 illustrates the progressive increase in resistance change ($\Delta R/R_0$) as the indentation depth increases.

Figure 32a shows real-time monitoring of resistance during indentation. The slight fluctuations in the data are attributed to aluminium foil wrinkling during the test, which momentarily disrupted contact and caused signal instability. Figure 32b presents processed results, showing a clear and smooth resistance increase curve. The resistance begins to rise immediately upon indentation, indicating that the MXene-coated structure is responsive from the very onset of mechanical deformation. At a 2 mm indentation depth, the resistance change exceeds 130%, confirming a strong electromechanical response. This suggests that MXene-coated honeycomb structures exhibit a strong self-sensing capability, making them promising for structural health monitoring applications.

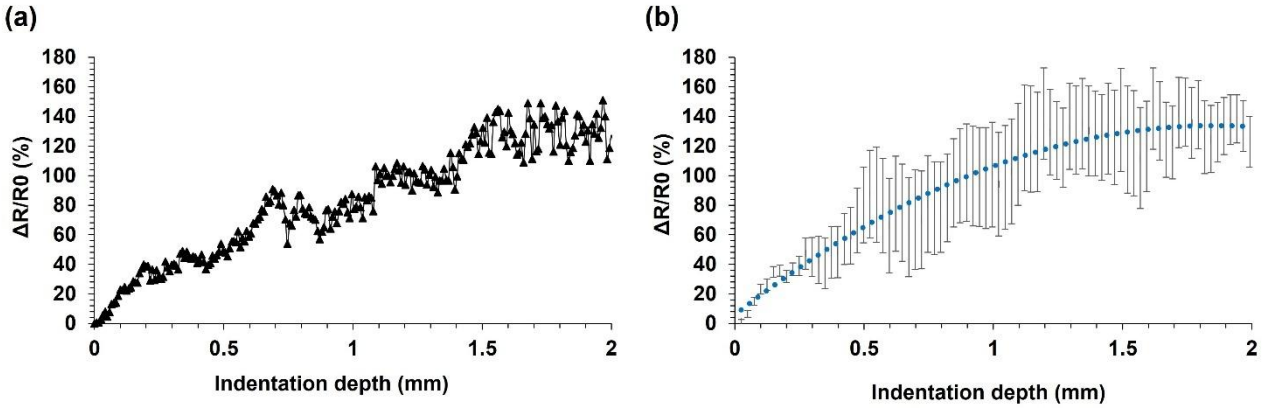

Fig. 32. Indentation response of honeycomb dip-coated with MXenes: a – real-time monitoring; b – processed and averaged results

The second experiment focused on a sandwich-structured composite where the GF was spray-coated with CNTs. The goal was to observe how this material system responds to increasing damage severity at the same location. As shown in Figure 33, two indenters of different diameters (1.5 cm and 5 cm) were applied sequentially at the same spot to evaluate the ability of the composite to detect progressive damage.

The 1.5 cm diameter indenter caused a resistance increase of up to approximately 2% after 4 mm of indentation depth. When the larger 5 cm indenter was applied to the same area, the resistance change rose to nearly 3% at the same depth, confirming that the material can detect increasing damage severity. However, it is important to note that both resistance changes are relatively low compared to the MXene-coated honeycomb structure, which reached a 130% resistance change under only 2 mm

of indentation. This indicates that the MXene-coated sample is more sensitive to mechanical damage, reacting immediately and with a significantly larger $\Delta R/R_0$ response. This difference in sensitivity is likely due to the structural properties of the MXene coating, which forms a dense and brittle network where conductive paths break more easily under stress. In contrast, the CNT network is more flexible, so small damage has less impact on its resistance.

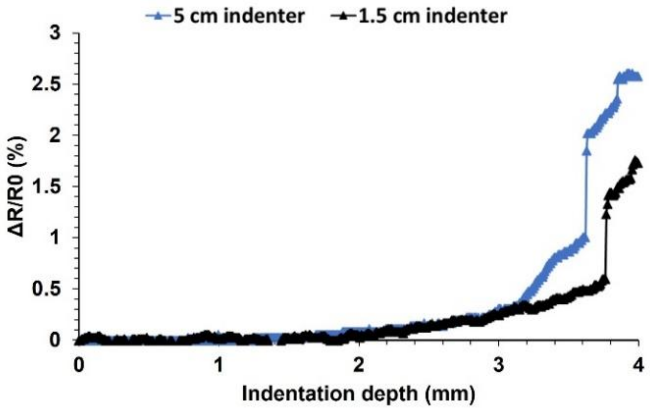

Fig. 33. Indentation response of GF spray-coated with CNT sandwich composite

To evaluate the performance of a composite system incorporating both CNT and MXene coatings, indentation tests were carried out on a self-sensing sandwich-structured composite featuring two independent sensing channels, A and B. Indentations were applied at 2 cm intervals along the length of the sample, and resistance responses were recorded independently in both channels to assess their localised sensing behaviour.

Figure 34 presents the resistance changes recorded by Channel A, which was positioned closer to the 0 cm end of the sample. The first indentation, located at 2 cm, resulted in a sharp resistance increase of 22%, as it was nearest to the channel. The second indentation at 4 cm led to a further increase to 25%. A smaller increase to 26% followed after the third indentation at 6 cm, while the fourth indentation at 8 cm which is outside the sensing range of Channel A did not produce any additional change.

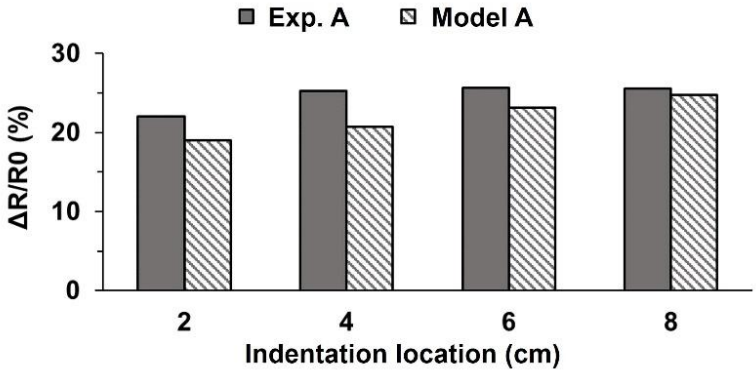

Fig. 34. Resistance change in Channel A during indentation at 2, 4, 6, and 8 cm positions

The analytical model closely replicated this trend but slightly underestimated the resistance values: it predicted increases of 19%, 21%, 23%, and 25% at the respective locations. The largest discrepancy occurred after the first indentation (a 3% difference), and the gap narrowed with increasing distance

from the channel. These deviations may be attributed to a non-uniform coating of nanomaterials, which alters current paths in the physical sample but is not accounted for in the analytical model.

Figure 35 shows the response from Channel B, positioned near the 10 cm end of the sample. The first indentation at 2 cm (farthest from Channel B) caused only a 2% resistance increase. The second indentation at 4 cm added just 1%, while the third at 6 cm closer to the channel triggered a more noticeable 8% rise. Finally, when the indentation was applied at 8 cm, directly adjacent to Channel B, the resistance rose sharply to 22%. This trend confirms that resistance changes become significantly larger as the damage approaches the sensing channel, with the response increasing in a clearly exponential manner.

The analytical model mirrored this trend well, though it slightly overestimated some values: it predicted increases of 2%, 3%, 6%, and 24%, respectively. The first result matched the experiment precisely, while the others were each about 2% higher. These findings validate the ability of the model to simulate the exponential growth in resistance as damage moves closer to the channel.

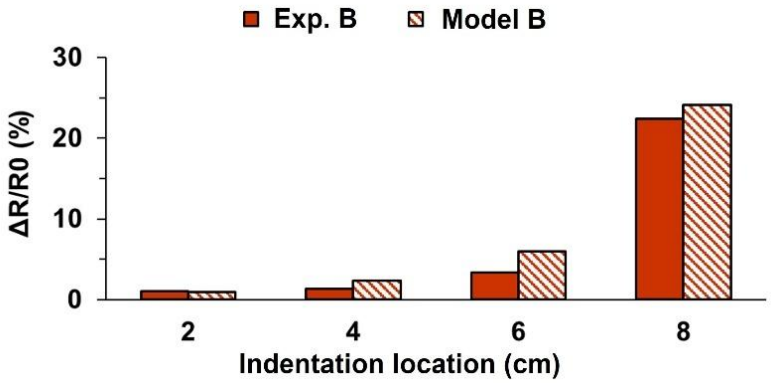

Fig. 35. Resistance change in Channel B during indentation at 2, 4, 6, and 8 cm position

Overall, the results show that the sandwich-structured composite demonstrates localised sensing behaviour: damage near a specific sensing channel causes a pronounced resistance increase, while damage beyond the channel's effective range has minimal effect. For example, at 2 cm, Channel A, being closest, showed a 22% resistance increase, while Channel B responded with only 2%. The analytical model successfully reflects this behaviour and can be used to predict spatial sensing performance. Minor differences between experimental and simulated results likely stem from practical factors such as non-uniform coating, material inconsistencies, or channel contact variations.

3.4.2. Delamination test

During the delamination test, the influence of GF layers spray-coated with CNTs detaching from the MXene-coated honeycomb core was evaluated in terms of electrical resistance response. As the delamination front progressed toward the sensing channel, the composite began to exhibit noticeable resistance changes.

Figure 36 shows that resistance increases exponentially with delamination length. Initially, up to about 20 mm, no significant change in resistance was observed, indicating that the delaminated region was outside the effective sensing range. However, once the delamination reached 20 mm, the resistance began to increase, reaching approximately 6%, as the damage entered the sensing field of the channel. As delamination continued to expand, the resistance rose more sharply climbing to 135%

at 45 mm. This substantial increase reflects the progressive disruption of the conductive pathways formed by the CNT-MXene network. Eventually, as the delamination length approaches full separation, the resistance tends toward a theoretical infinity, signalling a complete loss of electrical continuity between the layers and confirming full structural detachment.

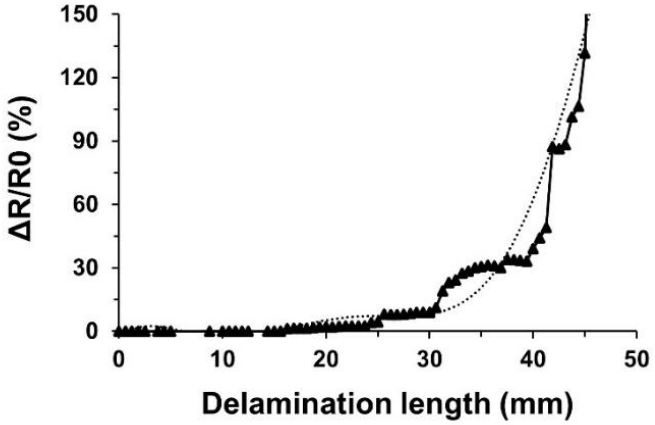

Fig. 36. Delamination test results

To further validate the sensing performance, Figure 37 compares experimental results with predictions from the analytical model. The model shows slightly higher sensitivity at early stages of delamination. For example, at 1 cm, the analytical model predicts a 6% resistance increase, whereas the experimental result is just 1%. At 2 cm, the model indicates a rise to 14%, while the experimental value reaches only 6%. This discrepancy could be due to idealised assumptions in the model, such as perfect nanoparticle distribution and full interfacial bonding, which are difficult to achieve in practice. Nevertheless, as delamination increases, both the experiment and model results show a maximum resistance at 5 cm, meaning the conductive networks are fully disconnected.

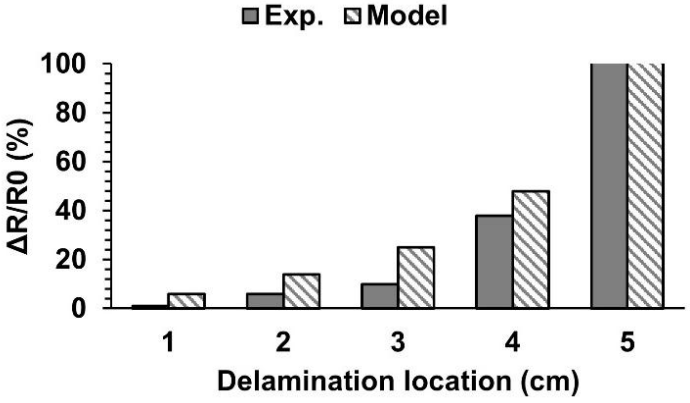

Fig. 37. Delamination test results comparison with analytical model

These findings confirm that as the delaminated area increases, so does the electrical resistance of the composite. The behaviour demonstrates a high degree of sensitivity to interfacial separation between layers, making the CNT/MXene-based composite a promising candidate for real-time structural health monitoring.

3.4.3. Three-point bending test

Three-point bending tests were performed to evaluate the electromechanical response of the composite under flexural loading. Figure 38 shows the relationship between the applied force and the resistance change as a function of extension. At the early stage of bending, the resistance remained nearly constant, with minimal change observed up to an extension of approximately 1.0 mm, when the applied force reached 52 N. Beyond this point, the resistance began to increase. As the extension reached 1.35 mm and the force rose to 65 N, the resistance change exceeded 10%, showing a rapid and exponential growth. This sharp rise suggests that the composite structure experiences significant internal changes, such as crack formation or interfacial stress transfer, which strongly affect the conductive pathways. These results confirm that the composite is capable of detecting bending-induced structural deformation in real-time.

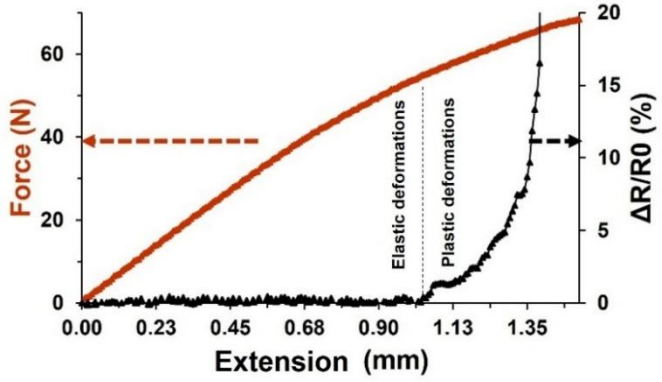

Fig. 38. Three-point bending test results

3.4.4. Temperature test

Aircraft operate in environments with highly variable temperatures, so it is essential to evaluate the electrical behaviour of the composite under different thermal conditions. To assess this, the composite was tested across a temperature range from –14 °C to +70 °C. As shown in Figure 39, the resistance demonstrated a clear temperature-dependent trend, decreasing steadily as the temperature increased.

Measurements were taken relative to a baseline at room temperature (20 °C). At the lowest tested temperature of –14 °C, the resistance increased by 27%. In contrast, at 70 °C, the resistance decreased by approximately 19%. In total, the relative resistance dropped by nearly 46% across the full temperature range.

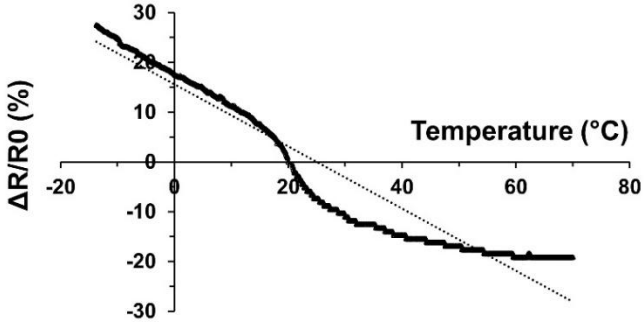

Fig. 39. Temperature test results

These results demonstrate that the electrical properties of the composite are highly sensitive to temperature. Temperature compensation or calibration may be necessary to ensure reliable performance in real-world conditions.

All conducted tests confirm that the sandwich-structured composite incorporating CNT and MXene nanoparticles is highly suitable for structural health monitoring (SHM) applications. The composite demonstrated the ability to detect and quantify various types of damage, including delamination, three-point bending, and indentation, as well as to track the progressive growth of such damage over time. Notably, the system also showed sensitivity to localised damage within the honeycomb core, such as debonding, buckling, and crack formation – failure modes that are often challenging to identify using conventional SHM techniques such as strain gauges or acoustic emission.

However, it should be noted that variations in nanoparticle distribution, caused by factors such as agglomeration and inconsistencies in the spray-coating or dip-coating processes, may affect the uniformity of the sensing layer. As a result, analytical model predictions may not always perfectly match experimental results, particularly in areas with uneven coating or disrupted conductive pathways. Future improvements in coating techniques and model calibration could help minimise these discrepancies and enhance prediction accuracy.

3.5. Real-time monitoring of a wing prototype

To evaluate the real-world applicability of the sandwich-structured composite, a wing prototype integrating six sensing channels was manufactured. Each has their sensing field in the composite structure. The electrical resistance of all six channels was continuously monitored using the “Arduino Cloud“ platform, which enabled real-time data visualisation.

Figure 40 presents the resistance behaviour of three bottom sensing channels, recorded immediately before and after one of the signal wires was intentionally disconnected. In the undamaged state (Figure 40a), all three channels showed stable and consistent resistance values, with only minor fluctuations. The yellow channel maintained a resistance of approximately 125 Ω, the orange channel around 150 Ω, and the red channel near 175 Ω.

After the intentional disconnection of the wire connected to the yellow channel (Figure 40b), its resistance instantly spiked toward infinity, indicating a complete loss of electrical continuity. At the same moment, a slight drop in resistance was observed in the orange and red channels. This could be related to sensing circuit rebalancing. However, the changes in these two channels were minimal compared to the yellow one, confirming that the event was localised and limited to a single electrical connection, not caused by mechanical damage in the structure.

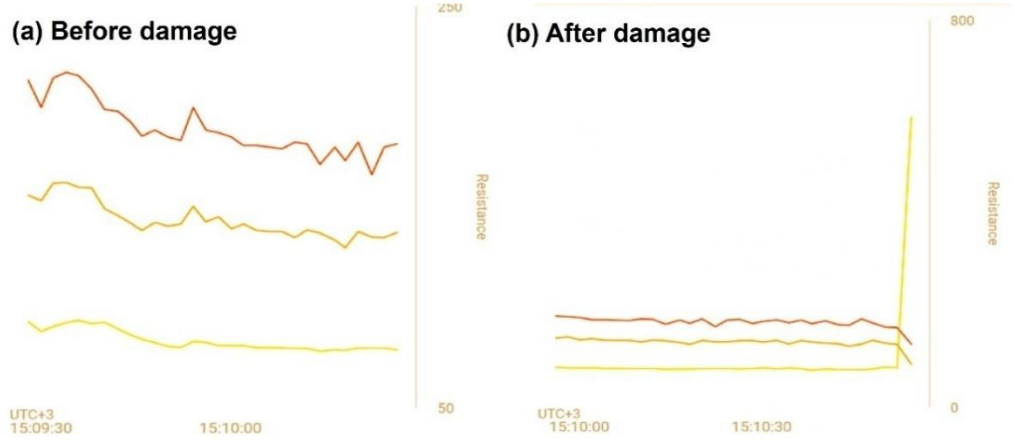

Fig. 40. Real-time resistance monitoring of the composite wing

This real-time resistance monitoring experiment demonstrated that the self-sensing sandwich-structured composite is effective and reliable in detecting localised structural damage. By continuously tracking the resistance of multiple sensing channels, the system can accurately identify which specific area is affected. This is especially valuable in aerospace applications, where early detection of defects is essential for flight safety and cost-efficient maintenance. The setup also provided clear insight into how the wing structure responds to electrical disruptions, showing that the system can dynamically monitor structural integrity during operation. Its ability to detect localised failure and provide real-time data makes it a promising solution for future smart aircraft components with built-in health monitoring capabilities.

Conclusions

1. Self-sensing composite was developed using honeycomb dip-coated MXene and PEDOT-CNT spray-coated glass fibre. Material characterisation using SEM showed the morphology of delaminated MXene with flake size reaching up to 5 μm, and single-walled CNT coatings. Electrical characterisation of MXenes showed that more dips lead to lower resistance. CNT average square centimetre resistance is 6 kΩ while honeycomb average values are 150 kΩ through the thickness.
2. The analytical model shows that the resistance sensitivity of the composite depends on the relative electrical conductivity of layers. Electrical resistance tends to increase slightly when the composite is damaged. The value of resistance increase is greater when the damage is closer to the channel, whereas damage further from the channel results in a lesser increase in resistance.
3. During the three-point bending test, after making 1.35 mm bend, a 20% resistance change was obtained. The delamination test showed that the resistance of the composite increases exponentially when the top glass fibre layer is gradually removed from the honeycomb. When the temperature changed from -14 ºC to +70 ºC, the relative resistance of the composite decreased by 50%.
4. The wireless self-diagnostic system created with the help of an "Arduino" microcontroller allows real-time monitoring of the condition of the composite and the propagation of damage.

List of references

1. Karsandik Y, Sabuncuoglu B, Yildirim B, Silberschmidt VV. Impact behavior of sandwich composites for aviation applications: A review. Compos Struct 2023;314:116941. https://doi.org/10.1016/j.compstruct.2023.116941.
2. Towsyfyan H, Biguri A, Boardman R, Blumensath T. Successes and challenges in non-destructive testing of aircraft composite structures. Chin J Aeronaut 2020;33:771–91. https://doi.org/10.1016/j.cja.2019.09.017.
3. Ogunleye RO, Rusnáková S, Javořík J, Žaludek M, Kotlánová B. Advanced Sensors and Sensing Systems for Structural Health Monitoring in Aerospace Composites. Adv Eng Mater 2024;26:2401745. https://doi.org/10.1002/adem.202401745.
4. Ayamga M, Akaba S, Nyaaba AA. Multifaceted applicability of drones: A review. Technol Forecast Soc Change 2021;167:120677. https://doi.org/10.1016/j.techfore.2021.120677.
5. Gundlach J. Designing unmanned aircraft systems: a comprehensive approach. Second edition. Reston, Virginia: American Institute of Aeronautics and Astronautics, Inc; 2014.
6. Ibrahim MohdR, Azman MF, Ariffin AH, Mansur MN, Mustapa MS, Irfan AR. Overview of Unmanned Aerial Vehicle (UAV) Parts Material in Recent Application. In: Ariffin AH, Latif NA, Mahmod MFB, Mohamad ZB, editors. Struct. Integr. Monit. Compos. Mater., Singapore: Springer Nature Singapore; 2023, p. 179–89. https://doi.org/10.1007/978-981-19-6282-0_11.
7. Yang H, Lee Y, Jeon S-Y, Lee D. Multi-rotor drone tutorial: systems, mechanics, control and state estimation. Intell Serv Robot 2017;10:79–93. https://doi.org/10.1007/s11370-017-0224-y.
8. Elijah T, Jamisola RS, Tjiparuro Z, Namoshe M. A review on control and maneuvering of cooperative fixed-wing drones. Int J Dyn Control 2021;9:1332–49. https://doi.org/10.1007/s40435-020-00710-2.
9. Benos L, Kateris D, Tagarakis AC, Bochtis D. Developments in the era of unmanned aerial systems. Unmanned Aer. Syst. Agric., Elsevier; 2023, p. 3–24. https://doi.org/10.1016/B978-0-323-91940-1.00001-3.
10. Galinski C, Hajduk J, Kalinowski M, Wichulski M, Stefanek Ł. Inverted joined wing scaled demonstrator programme. 29th Congr Int Counc Aeronaut Sci ICAS 2014 n.d.
11. BAYKAR. (2023). Bayraktar tb3 siha cumhuriyetimizin 100. yilinda gökyüzüyle buluştu [viewed 30 January 2025]. Retrieved from https://baykartech.com/tr/haberler/bayraktar-tb3-siha-cumhuriyetimizin-100-yilinda-gokyuzuyle-bulustu/.
12. Kunertova D. Learning from the Ukrainian Battlefield: Tomorrow's Drone Warfare, Today's Innovation Challenge. ETH Zurich; 2024. https://doi.org/10.3929/ETHZ-B-000690448.
13. Saeed AS, Younes AB, Cai C, Cai G. A survey of hybrid Unmanned Aerial Vehicles. Prog Aerosp Sci 2018;98:91–105. https://doi.org/10.1016/j.paerosci.2018.03.007.
14. Sonkar S, Kumar P, George RC, Yuvaraj TP, Philip D, Ghosh AK. Low-cost development of a fully composite fixed-wing hybrid VTOL UAV. J Braz Soc Mech Sci Eng 2024;46:252. https://doi.org/10.1007/s40430-024-04785-2.
15. Guo H, Yuan H, Zhang J, Ruan D. Review of sandwich structures under impact loadings: Experimental, numerical and theoretical analysis. Thin-Walled Struct 2024;196:111541. https://doi.org/10.1016/j.tws.2023.111541.
16. Ma W, Elkin R. Sandwich Structural Composites: Theory and Practice. 1st ed. Boca Raton: CRC Press; 2021. https://doi.org/10.1201/9781003035374.

17. Mouritz AP. Introduction to aerospace materials. Oxford (GB): Woodhead publ; 2012.
18. Gurgen S. Modern Manufacturing Processes for Aircraft Materials. 1st ed. San Diego: Elsevier; 2023.
19. Karsandik Y, Sabuncuoglu B, Yildirim B, Silberschmidt VV. Impact behavior of sandwich composites for aviation applications: A review. Compos Struct 2023;314:116941. https://doi.org/10.1016/j.compstruct.2023.116941.
20. S. N. Abhinav, Maharaja Vijayaram Gajapathi Raj college of engineering. A Review Paper on Origin of Honeycomb Structure and its Sailing Properties. Int J Eng Res 2020;V9:IJERTV9IS080336. https://doi.org/10.17577/IJERTV9IS080336.
21. Pütz M, Lafont U, Wittlich M, Markestein E, Herrmann C, Fischer H. 3D honeycomb for advanced manufacturing for space application. CEAS Space J 2023;15:203–11. https://doi.org/10.1007/s12567-022-00444-1.
22. Jaafar M, Makich H, Nouari M. A new criterion to evaluate the machined surface quality of the Nomex® honeycomb materials. J Manuf Process 2021;69:567–82. https://doi.org/10.1016/j.jmapro.2021.07.062.
23. Zaed M, Cherusseri J, Tan KH, Saidur R, Pandey AK. Hierarchical Ti3C2Tx MXene@Honeycomb nanocomposite with high energy efficiency for solar water desalination. Chemosphere 2024;366:143459. https://doi.org/10.1016/j.chemosphere.2024.143459.
24. Takeda N, Minakuchi S, Okabe Y. Smart Composite Sandwich Structures for Future Aerospace Application -Damage Detection and Suppression-: a Review. J Solid Mech Mater Eng 2007;1:3–17. https://doi.org/10.1299/jmmp.1.3.
25. Grigoriou K, Ladani RB, Mouritz AP. Electrical properties of multifunctional Z-pinned sandwich composites. Compos Sci Technol 2019;170:60–9. https://doi.org/10.1016/j.compscitech.2018.11.030.
26. Jovarauskaite G, Monastyreckis G, Mishnaevsky L, Zeleniakiene D. Self-sensing composites with damage mapping using 3D carbon fibre grid. Compos Part B Eng 2025;295:112182. https://doi.org/10.1016/j.compositesb.2025.112182.
27. Xu X, Ran B, Jiang N, Xu L, Huan P, Zhang X, et al. A systematic review of ultrasonic techniques for defects detection in construction and building materials. Measurement 2024;226:114181. https://doi.org/10.1016/j.measurement.2024.114181.
28. Wilson CL, Lonkar K, Roy S, Kopsaftopoulos F, Chang F-K. 7.20 Structural Health Monitoring of Composites. Compr. Compos. Mater. II, Elsevier; 2018, p. 382–407. https://doi.org/10.1016/B978-0-12-803581-8.10039-6.
29. Rocha H, Semprimoschnig C, Nunes JP. Sensors for process and structural health monitoring of aerospace composites: A review. Eng Struct 2021;237:112231. https://doi.org/10.1016/j.engstruct.2021.112231.
30. Kosova F, Altay Ö, Ünver HÖ. Structural health monitoring in aviation: a comprehensive review and future directions for machine learning. Nondestruct Test Eval 2025;40:1–60. https://doi.org/10.1080/10589759.2024.2350575.
31. Peters K, Inaudi D. Optical fibre sensors. Sens. Technol. Civ. Infrastruct., Elsevier; 2022, p. 113–47. https://doi.org/10.1016/B978-0-08-102696-0.00005-1.
32. Mangi MA, Elahi H, Ali A, Jabbar H, Aqeel AB, Farrukh A, et al. Applications of Piezoelectric-based Sensors, Actuators, and Energy Harvesters. Sens Actuators Rep 2025:100302. https://doi.org/10.1016/j.snr.2025.100302.

33. Firoozi AA, Firoozi AA. Emerging Trends in Damage Tolerance Assessment: A Review of Smart Materials and Self-Repairable Structures. Struct Durab Health Monit 2024;18:1–18. https://doi.org/10.32604/sdhm.2023.044573.
34. Anbusagar NRR, Palanikumar K, Ponshanmugakumar A. Preparation and properties of nanopolymer advanced composites: A review. Polym.-Based Nanocomposites Energy Environ. Appl., Elsevier; 2018, p. 27–73. https://doi.org/10.1016/B978-0-08-102262-7.00002-7.
35. Ali Z, Yaqoob S, Yu J, D'Amore A. Critical review on the characterization, preparation, and enhanced mechanical, thermal, and electrical properties of carbon nanotubes and their hybrid filler polymer composites for various applications. Compos Part C Open Access 2024;13:100434. https://doi.org/10.1016/j.jcomc.2024.100434.
36. Rani P, Ahamed MB, Deshmukh K. Carbon Nanotubes Embedded in Polymer Nanofibres by Electrospinning. In: Abraham J, Thomas S, Kalarikkal N, editors. Handb. Carbon Nanotub., Cham: Springer International Publishing; 2022, p. 943–77. https://doi.org/10.1007/978-3-030-91346-5_12.
37. Siahkouhi M, Razaqpur G, Hoult NA, Hajmohammadian Baghban M, Jing G. Utilization of carbon nanotubes (CNTs) in concrete for structural health monitoring (SHM) purposes: A review. Constr Build Mater 2021;309:125137. https://doi.org/10.1016/j.conbuildmat.2021.125137.
38. Qiu H, Yang J. Structure and Properties of Carbon Nanotubes. Ind. Appl. Carbon Nanotub., Elsevier; 2017, p. 47–69. https://doi.org/10.1016/B978-0-323-41481-4.00002-2.
39. Meyyappan M, editor. Carbon nanotubes: science and applications. Boca Raton, Fla.: CRC Press; 2005.
40. Ding S, Xiang Y, Ni Y-Q, Thakur VK, Wang X, Han B, et al. In-situ synthesizing carbon nanotubes on cement to develop self-sensing cementitious composites for smart high-speed rail infrastructures. Nano Today 2022;43:101438. https://doi.org/10.1016/j.nantod.2022.101438.
41. Qin H, Ding S, Ashour A, Zheng Q, Han B. Revolutionizing infrastructure: The evolving landscape of electricity-based multifunctional concrete from concept to practice. Prog Mater Sci 2024;145:101310. https://doi.org/10.1016/j.pmatsci.2024.101310.
42. Li L, Wei H, Hao Y, Li Y, Cheng W, Ismail YA, et al. Carbon nanotube (CNT) reinforced cementitious composites for structural self-sensing purpose: A review. Constr Build Mater 2023;392:131384. https://doi.org/10.1016/j.conbuildmat.2023.131384.
43. Zeng X, Cheng X, Yu R, Stucky GD. Electromagnetic microwave absorption theory and recent achievements in microwave absorbers. Carbon 2020;168:606–23. https://doi.org/10.1016/j.carbon.2020.07.028.
44. Li W, Huang Y, Liu Y, Tekell MC, Fan D (Emma). Three dimensional nanosuperstructures made of two-dimensional materials by design: Synthesis, properties, and applications. Nano Today 2019;29:100799. https://doi.org/10.1016/j.nantod.2019.100799.
45. Deshmukh K, Pandey M, Hussain CM, editors. MXene reinforced polymer composites: fabrication, characterization and applications. Hoboken, NJ: Wiley; 2024. https://doi.org/10.1002/9781119901280.
46. Chakraborty P, Das T, Saha-Dasgupta T. MXene: A New Trend in 2D Materials Science. Compr. Nanosci. Nanotechnol., Elsevier; 2019, p. 319–30. https://doi.org/10.1016/B978-0-12-803581-8.10414-X.

47. Salim O, Mahmoud KA, Pant KK, Joshi RK. Introduction to MXenes: synthesis and characteristics. Mater Today Chem 2019;14:100191. https://doi.org/10.1016/j.mtchem.2019.08.010.
48. Sivasubramaniyam V, Ramasamy S, Venkatraman M, Gatto G, Kumar A. Carbon Nanotubes as an Alternative to Copper Wires in Electrical Machines: A Review. Energies 2023;16:3665. https://doi.org/10.3390/en16093665.
49. Ghamsarizade R, Ramezanzadeh B, Mohammadloo HE. A review on recent advances in 2D-transition metal carbonitride-MXenes nano-sheets/polymer composites' electromagnetic shields, mechanical and thermal properties. J Taiwan Inst Chem Eng 2023;144:104740. https://doi.org/10.1016/j.jtice.2023.104740.
50. Grabowski K, Srivatsa S, Vashisth A, Mishnaevsky L, Uhl T. Recent advances in MXene-based sensors for Structural Health Monitoring applications: A review. Measurement 2022;189:110575. https://doi.org/10.1016/j.measurement.2021.110575.
51. Chi G, Xu S, Yu D, Wang Z, He Z, Wang K, et al. A brief review of structural health monitoring based on flexible sensing technology for hydrogen storage tank. Int J Hydrog Energy 2024;80:980–98. https://doi.org/10.1016/j.ijhydene.2024.07.215.
52. Arduino. Nano ESP32. Arduino Store [viewed 30 January 2025]. Retrieved from https://store.arduino.cc/products/nano-esp32.

Appendices

Appendix 1. Code for wing's real-time monitoring

```
//   SENOSR 0
const int sensorPinA0 = A0;  // Analog input pin that senses Vout
int sensorValue0 = 0;        // sensorPin default value
float Vin0 = 3.3;            // Input voltage
float Vout0 = 0;             // Vout default value
float Rref0 = 100;           // Reference resistor's value in ohms
float R0 = 0;                // Tested resistors default value

//  SENOSR 1
const int sensorPinA1 =A1;
int sensorValue1 = 0;
float Vin1 = 3.3;
float Vout1 = 0;
float Rref1 = 100;
float R1 = 0;

//     SENOSR 2
const int sensorPinA2 = A2;
int sensorValue2 = 0;
float Vin2 = 3.3;
float Vout2 = 0;
float Rref2 = 100;
float R2 = 0;

//  SENOSR 3
const int sensorPinA3 = A2+1;
```

```
int sensorValue3 = 0;
float Vin3 = 3.3;
float Vout3 = 0;
float Rref3 = 100;
float R3 = 0;

//   SENOSR 4
const int sensorPinA4 = A2+2;
int sensorValue4 = 0;
float Vin4 = 3.3;
float Vout4 = 0;
float Rref4 = 100;
float R4 = 0;

//  SENOSR 5
const int sensorPinA5 = A2+3;
int sensorValue5 = 0;
float Vin5 = 3.3;
float Vout5 = 0;
float Rref5 = 100;
float R5 = 0;
void setup ()
{
  Serial.begin(115200);      // Initialize serial communications at 115200 bps
}
void loop ()
{
  Serial.print("A0:");
```

```
  Serial.print(A0);
  Serial.println("");
  delay(50);

 //   SENOSR 0
  sensorValue0 = analogRead(sensorPinA0);  // Read Vout on analog input pin A0
  Vout0 = (Vin0 * sensorValue0) / 1023;    // Convert Vout to volts
  R0 = -1*Rref0 *(1/((Vin0 / Vout0) - 1));  // Formula to calculate tested resistor's value

 //  SENOSR 1
  sensorValue1 = analogRead(sensorPinA1);
  Vout1 = (Vin1 * sensorValue1) / 1023;
  R1 = -1*Rref1 * (1 / ((Vin1 / Vout1) - 1));

//  SENOSR 2
  sensorValue2 = analogRead(sensorPinA2);
  Vout2 = (Vin2 * sensorValue2) / 1023;
  R2 = -1*Rref2 * (1 / ((Vin2 / Vout2) - 1));

 //  SENOSR 3
  sensorValue3 = analogRead(sensorPinA3);
  Vout3 = (Vin3 * sensorValue3) / 1023;
  R3 = -1*Rref3 * (1 / ((Vin3 / Vout3) - 1));

//  SENOSR 4
  sensorValue4 = analogRead(sensorPinA4);
  Vout4 = (Vin4 * sensorValue4) / 1023;
  R4 = -1*Rref4 * (1 / ((Vin4 / Vout4) - 1));
```

```
  //  SENOSR 5
  sensorValue5 = analogRead(sensorPinA5);
  Vout5 = (Vin5 * sensorValue5) / 1023;
  R5 = -1*Rref5 * (1 / ((Vin5 / Vout5) - 1));
  // All channels Serial print: Give calculated resistance in Serial Monitor
 Serial.print(R0); Serial.print(",");
 Serial.print(R1); Serial.print(",");
 Serial.print(R2); Serial.print(",");
 Serial.print(R3); Serial.print(",");
 Serial.print(R4); Serial.print(",");
 Serial.println(R5); Serial.print(",");    //
  delay(50);                        // Delay in milliseconds between reeds
}
```